structural details of the antibody mode of binding to the VLPs, S domain or P domain, have been lacking. In the studies presented here, we used X-ray crystallography to define the recognition site of the broadly reactive antibody 5B18 on the norovirus GII.10 P domain, cryo-EM to determine the structure of the intact GII.10 VLP, and ELISA to determine whether this antibody recognizes intact or disassembled virus particles. Overall, the findings have implications related to the dynamic nature of the P domain in the context of the norovirus VLP and to its recognition by antibody.

MATERIALS AND METHODS

Norovirus VLP expression. The GII.4 Saga (GenBank accession number BAG70515), GII.10 Vietnam026 (GenBank accession number AF504671) (23), and GII.12 Hiro (GenBank accession number AB044366) (23) VLPs were expressed as previously described (23). The VLPs were purified using CsCl equilibrium gradient ultracentrifugation at 35,000 rpm for 24 h at 4°C (Beckman SW55 rotor). A distinct viral band was removed from the side of the tube with a syringe and the VLPs were stored in phosphate-buffered saline (PBS) (pH 7.3) at 4°C. The integrity of the VLPs was confirmed by negative-stain EM. Briefly, the VLP samples were applied to a carbon-coated 300-mesh EM grid and stained with 2% uranyl acetate (pH 4). Grids were examined using a Jeol JEM-1220 transmission electron microscope operated at 80 kV.

Antibody ELISA binding to GII.4, GII.10, and GII.12 VLPs. An antibody ELISA was used to compare the cross-reactivities of VLPs from the three different GII norovirus genotypes (GII.4, GII.10, and GII.12) with 5B18 IgG. Wells of 96-well microtiter plates (MaxiSorp; Nunc, Denmark) were each coated with 100 μl of ~100 ng of purified VLPs (in PBS, pH 7.3) and incubated overnight at 4°C. The wells were washed four times with PBS containing 0.1% (vol/vol) Tween 20 (PBS-T) and then were blocked with PBS containing 5% (wt/vol) skim milk for 1 h at room temperature. After the wells were washed four times with PBS-T, 100 μl of 2-fold serially diluted horseradish peroxidase (HRP)-conjugated labeled 5B18 IgG, from a 1:5,000 starting dilution in PBS containing 0.05% (wt/vol) skim milk, was added to each well, and the plates were incubated for 1 h at 37°C. The wells were washed four times with PBS-T, and then 100 μl of 3,3′,5,5′-tetramethylbenzidine substrate was added to each well. The reaction was stopped by the addition of 100 μl of 2 N H_2SO_4 to each well, and the absorbance was measured at 450 nm (A_{450}). The titer was expressed as the reciprocal of the highest dilution of antiserum giving a value of A_{450} of >0.2, as previously described (21).

Western blotting. The VLPs and P domains were separated by SDS-PAGE and electrotransferred to polyvinylidene difluoride (PVDF) membranes by using iBLOT, following the manufacturer's protocol. Proteins were detected with 5B18 IgG at a dilution of 1:5,000, and then, following the manufacturer's instructions, the blots were developed by chemiluminescence using enhanced chemiluminescence (ECL) detection reagent (Amersham Biosciences, England).

Protein expression and purification of GII.10 P domain. The GII.10 P domain was expressed in *E. coli* and purified as previously described (22). Briefly, the P domain was optimized for *E. coli* expression, cloned in a modified pMal-c2x vector at the BamHI and NotI restriction sites (New England BioLabs), and transformed into BL21(DE3) cells (Invitrogen). Expression was induced with IPTG (isopropyl-β-D-thiogalactopyranoside) (1 mM) for 18 h at 22°C. After a series of purification steps and protease cleavage, the P domain was concentrated to 2 to 10 mg/ml and stored in gel filtration buffer (0.35 M NaCl, 2.5 mM Tris, pH 7.0, 0.02% NaN_3).

Preparation of 5B18 Fab fragment. The 5B18 IgG monoclonal antibody was produced from a mouse immunized with GII.4 norovirus-445 VLPs (GenBank accession number DQ093064) (Denkaseiken, Japan). The 5B18 IgG is currently used as a GII broad-range capture antibody in a commercially available ELISA kit (Denkaseiken, Japan). The 5B18 Fab was prepared using a modified method (34). Approximately 60 mg of purified 5B18 IgG was used for Fab preparation. IgG was reduced in 100 mM dithiothreitol (DTT) (pH 7.6) for 1 h at 37°C. The reduced IgG was added to a dialysis cassette, and the DTT was removed by placing the cassette in GFB (0.35 M NaCl, 2.5 mM Tris, pH 7.0, 0.02% NaN_3) supplemented with 20 mM HEPES (pH 7.7) for 1 h at 4°C. The IgG was alkylated in the same buffer supplemented with 2 mM iodoacetamide for 48 h at 4°C, and then the cassette was transferred to a fresh solution without the iodoacetamide for 1 h at 4°C. The IgG was concentrated to 5 mg/ml and then digested with papain using a commercial kit (Pierce, Rockford, United States). The Fab was separated from the Fc in a protein A column, and the resulting Fab was further purified by size exclusion chromatography with a Superdex 200 column (GE), concentrated to 5 mg/ml, and stored in GFB. The purified GII.10 P domain and Fab were mixed 1.4:1 for 1 h at 25°C, and finally, the GII.10 P domain-Fab complex was purified by size exclusion chromatography.

Preparation and cocrystallization of GII.10 P domain-Fab complex for X-ray crystallography. Crystals of the GII.10 P domain-Fab complex were grown by the hanging drop vapor diffusion method, mixing the protein and reservoir solution (40% [vol/vol] polyethylene glycol [PEG] 400, 5% [wt/vol] PEG 3350, and 0.1 M acetic acid, pH 5.5) (42) in a 1:1 ratio. Crystals grew over 1 week at a temperature of 20°C. Prior to data collection, crystals were transferred to 50% (vol/vol) PEG 400.

X-ray crystallography data collection, structure solution, and refinement. X-ray diffraction data were collected at the Southeast Regional Collaborative Access Team (SER-CAT) beamline 22-BM at the Advanced Photon Source, Argonne National Laboratory, Argonne, IL, and processed with HKL2000 (49). Despite the large size of the crystals (perfectly formed pyramids of up to 0.3 mm per edge), the diffraction data were poor due to split reflections, high background, and most diffraction extending to less than 4 Å. These resulted in Chi^2 values of 0 for several wedges of data. Despite these difficulties, relatively complete data (90%) was obtained from 180 degrees of oscillation, though with lower than expected redundancy (2.7-fold), and the overall quality of data which passed the Chi^2 tests appeared fine. Structures were solved by molecular replacement in PHASER (44), using the structure with Protein Data Bank identifier (PDB ID) 3ONU for the GII.10 P domain and the structure with PDB ID 1WEJ for the Fab as a search model. Manual model building was performed in COOT (18), and positional refinement together with translation/liberation/screw (TLS) refinement were performed using REFMAC (14) and PHENIX (1).

Cryo-EM data collection and refinement. VLPs at a concentration of 1.0 mg/ml were applied to a glow-discharged Quantifoil R1.2/1.3 Mo 200-mesh holey carbon grid with a thin layer of carbon over the holes. The sample was rapidly plunged into liquid ethane after automatic blotting for 7 to 8 s at 8°C and 100% humidity using an FEI MarkIV Vitrobot. Grids were examined with a JEOL JEM-2200FFC microscope equipped with a field emission gun and an in-column (omega-type) energy filter operated at an acceleration voltage of 200 kV. Images of the frozen VLPs were collected at a nominal magnification of 40,000 using a 4k × 4k (4,096- by 4,096-pixel) Tietz charge-coupled-device (CCD) camera, resulting in a pixel size of 2.4 Å. Particles were extracted from raw micrographs using the swarm semiautomatic particle-picking algorithm in EMAN2 into boxes of 250 by 250 square pixels (61). The raw particles were normalized, phase flipped, and high-pass filtered before single-particle analysis. Approximately 8,000 particle images were subjected to two-dimensional (2-D) reference-free alignment and classification through several rounds of multireference alignment and multivariate statistical analysis in IMAGIC to a total of 50 classes (65). Approximately 80% of the data were used for the reconstruction. Particles with cross-correlation values 1.5 σ below the mean were not used (~20%). Representative class averages were used as the basis for initial model generation in EMAN2. The initial model with the best match between reprojections and class averages was chosen as the starting model for several rounds of projection-matching refinement with increasing angular sampling. The final reconstruction, at ~10-Å resolution (0.5 Fourier shell correlation [FSC] criterion), was used for atomic coordinate fitting and structure comparison in Chimera (version 1.5.3) (52).

Structure analysis, sequence analysis, and figures. Figures were rendered using PyMOL (version 1.2r3; Schroedinger LLC) and Chimera (version 1.5.3) (52). The N-terminal amino acid sequences for the Fab heavy and kappa (κ) chains were determined at the Columbia University Medical Center, Protein Core Facility. Degenerate primers for the Fab sequence were designed from constant regions and from the N-terminal amino acid sequence based on closely matching murine antibody N-terminal nucleotide sequences in GenBank. Norovirus complete-capsid amino acid sequences were aligned and analyzed with GenetyxMac software (version 16.0.0).

Antibody ELISA binding to GII.10 VLPs at different pHs. An antibody ELISA was used to determine the ability of 5B18 IgG to bind to GII.10 VLPs. The GII.10 VLPs were diluted in PBS at pHs 5.3, 6.3, 7.3, 8.3, and 9.3 to a final concentration of 7.5 μg/ml. At high PBS pHs, the VLPs were found to be partially broken, while at low pHs, most of the VLPs were intact. Wells of 96-well microtiter plates (MaxiSorp; Nunc, Denmark) were each coated with 100 μl of 7.5 μg/ml of VLPs at the different pHs and incubated overnight at 4°C. The VLPs were detected as described above, except that 5B18 IgG and goat HRP–anti-mouse IgG (used as a secondary antibody) replaced the HRP-labeled 5B18 IgG. After the addition of the secondary antibody, the wells were washed four times with PBS-T, and then 100 μl of substrate *o*-phenylenediamine and H_2O_2 was added to each well and the plates left in the dark for 30 min at room temperature. The reaction was stopped by the addition of 50 μl of 2 N H_2SO_4 to each well, and the absorbance was measured at 492 nm (A_{492}).

Sequence conservation on the VLP and P domain. To show the sequence conservation on the GII VLP, a model of the GII.10 VLP was built as described previously (22) using the unbound GII.10 P domain structure (PDB ID 3ONU) and the S domain from the Norwalk virus capsid structure (PDB ID 1IHM). Amino acid sequence conservation was analyzed as previously described (22). Briefly, an alignment of a representative set of GII sequences was used to compute residue conservation scores using the AL2CO server (51) and mapped (using a color range for highly variable to highly conserved residues) onto the surface of the GII.10 VLP model and unbound GII.10 P domain structure.

Accession numbers. Atomic coordinate and structure factors of the X-ray crystal structure were deposited in the Protein Data Bank under accession number 3V7A. The 3-D cryo-EM map was deposited in the EMDataBank with accession number EMD-5374.

RESULTS

5B18 binds to several GII genotypes. To confirm the ability of the 5B18 IgG to bind diverse GII norovirus genotypes, we expressed VLPs from three GII genotypes (GII.4, GII.10, and GII.12) and examined the binding using ELISA and Western blotting. The EM results showed that GII.4 VLPs were a mixture of small and native-size particles, while the GII.10 and GII.12 VLPs were mostly of native size (data not shown). The ELISA results showed that 5B18 IgG was capable of cross-reacting with all three GII genotypes having an equal titer of 320,000 (see Fig. S1A in the supplemental material). The Western blotting results also showed that the 5B18 IgG could detect the three GII genotypes (see Fig. S1B).

X-ray crystal structure of GII.10 P domain-Fab complex. The GII.10 P domain was used to determine the precise binding location of the 5B18 antibody on the norovirus capsid using X-ray crystallography. The GII.10 P domain and Fab proteins were mixed together (1.4:1 molar ratio) for 1 h at room temperature. The GII.10 P domain-Fab complex was purified using size exclusion chromatography. Two main peaks were observed, corresponding to the complex and free P domain (data not shown). The fractions containing the GII.10 P domain-Fab complex were pooled and concentrated to ~4 mg/ml, and the complex was crystallized by the hanging-drop vapor diffusion method. A single GII.10 P domain-Fab complex crystal diffracted X rays to ~3.3 Å. The structure was solved using molecular replacement with a GII.10 P domain monomer (PDB ID 3ONU) and a mouse Fab (PDB ID 1WEJ) as search models. Molecular replacement indicated that two P domain monomers and two 5B18 Fabs each containing a kappa (κ) chain and heavy chain were in the asymmetrical unit and these were related by a noncrystallographic 2-fold. Water molecules were not added to the structure since the resolution was at 3.3 Å. The 5B18 Fab was shown to bind to the wall of the P1 subdomain and involved a monomeric interaction with the P1 subdomain (Fig. 1A). The electron densities of the P domains and 5B18 Fabs were generally well defined, and refinement led to an R_{value} of 0.230 (R_{free} of 0.283) (Table 1; also see Fig. S2 in the supplemental material). The P domain dimer had a single helix in each P1 subdomain and six antiparallel β-strands in each P2 subdomain as previously described (22).

GII.10 P domain interaction with the 5B18 Fab. The total interface area of the GII.10 P domain and 5B18 Fab was 1,500 Å^2 (770 Å^2 on the P domain and 730 Å^2 on the 5B18 Fab), as calculated using PISA software (33). The GII.10 P domain and 5B18 Fab interaction included nine hydrogen bonds, eight of which were formed between the P1 subdomain and κ chain and one between the P1 subdomain and heavy chain (Fig. 1B; also see Table S1 in the supplemental material). Six P1 subdomain amino acids interacted with the 5B18 Fab, Tyr533 formed a single hydrogen bond with Tyr92κ, Thr534 formed three hydrogen bonds with Gly93κ and one hydrogen bond with Trp97κ, Leu535 formed a hydrogen bond with Tyr32κ, Glu496 formed a hydrogen bond with Tyr92κ, Asn530 formed a hydrogen bond with Ser94κ, and Val433 formed a hydrogen bond with Asn52 heavy chain. Superposition of the apo GII.10 P domain dimer and the Fab-bound GII.10 P domain showed that each of the P1 subdomains shifted slightly (~1 to 2 Å) toward the center of the dimer, while the P2 subdomain showed little conformational change (see Fig. S3 in the supplemental material). The electrostatic potential of the Fab was calculated (16), and the interacting residues on the P domain bound at two negatively charged pockets on the Fab at the variable regions (Fig. 2).

Conservation of the 5B18 Fab-binding site on GII P domains. The 5B18 Fab formed hydrogen bonds with residues at three different sites on the P1 subdomain, termed A, B, and C (Fig. 3). An amino acid alignment of representatives from 10 GII norovirus genotypes indicated that Val433 (site A) was the most variable, with other genotypes having threonine, serine, asparagine, leucine, or methionine at this position. Thr534 (site C) was mostly conserved, as the only other amino acid at this position was a serine. Glu496 (site B), Asn530 (site C), Tyr533 (site C), and Leu535 (site C) were all highly conserved among the representative GII genotypes. Superposition of other known GII norovirus P domains (GV.1, GII.4-TCH05, GII.4-VA387, GII.12, GII.9-VA207, and GI.1) showed that the equivalent GII.10 interacting side chains were mostly in the same conformation (see Fig. S4 in the supplemental material). GI norovirus side chains also appeared to be similar to the GII.10 interacting side chains (see Fig. S4).

GII.10 VLP cryo-EM structure. From the general location of the epitope (Fig. 1) and the known structures of other caliciviruses (7, 10, 13, 22), it was not clear how the monoclonal antibody, raised against intact VLPs, could bind at this occluded site on intact particles. To this end, the cryo-EM structure of the GII.10 VLP (in an unbound state) was determined to define the arrange-

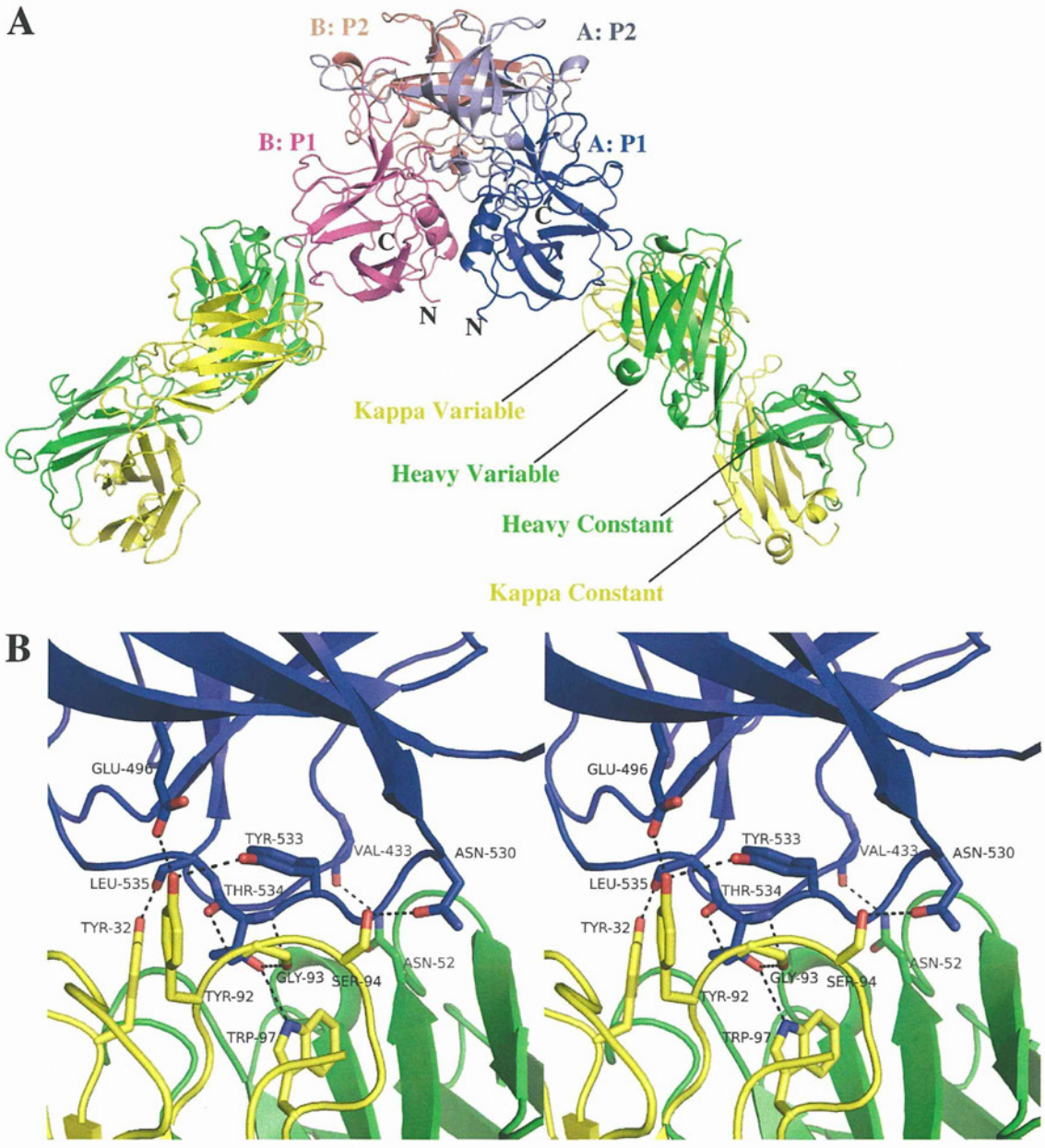

FIG 1 The X-ray crystal structure of the GII.10 P domain-Fab complex shows that the Fab bound to the lower side of the P1 subdomain. The GII.10 P domain dimer is colored according to monomers and subdomains, i.e., chain A: P1 (blue), chain A: P2 (light blue), chain B: P1 (violet), and chain B: P2 (salmon), whereas the Fab is colored according to chain, i.e., κ chain (yellow) and heavy chain (green). (A) The Fab bound to the wall of the P1 subdomain (considered to be inside the virus particle) and involved a monomeric interaction. (B) A close-up stereoview of the interacting P domain residues for chain A (Val433, Glu496, Asn530, Tyr533, Thr534, and Leu535) and Fab residues (κ chain, Tyr32, Tyr92, Gly93, Ser94, and Trp97, and heavy chain, Asn52). The hydrogen bond interactions included both side chain and main chain interactions (also see Table S1 in the supplemental material).

ment of the GII.10 P domains with respect to the entire capsid. The GII.10 VLPs appeared as homogeneous, monodisperse particles in ice (see Fig. S5A in the supplemental material). Reference-free class averages of the VLPs showed icosahedral particles with spike-like structures extending from the vertices (see Fig. S5). The cryo-EM reconstruction of the GII.10 VLP at ~10-Å resolution (0.5 FSC criterion) showed several striking features (Fig. 4). The GII.10 S domain was noticeably surface exposed at the 3- and 5-fold axes (Fig. 4A). The GII.10 P domain appeared as a second outer shell, and a central section through the VLP revealed that the P domain was raised off the S domain by ~15 Å (Fig. 4B). The electron density at the tip of the P domain (the P2 subdomain) was significantly weaker than at the base of the P1 domain, suggesting that there was marked flexibility in the P2 subdomains. This was consistent with what has been observed with several other reconstructions of calicivirus particles (4, 5) and suggests that there is a great deal of conformational heterogeneity in the P domains.

Fitting of the GII.10 P domain and P domain-Fab complex into the GII.10 VLP cryo-EM structure. At ~10-Å resolution, the GII.10 P domain monomers on the VLP were easily distinguished.

TABLE 1 Data collection and refinement statistics for the GII.10 norovirus P domain-Fab complex structure

Parameter	Value[a]
Data collection	
Space group	$P\,4_322$
Cell dimensions	
a, *b*, *c* (Å)	145.48, 145.48, 216.33
α, β, γ (°)	90, 90, 90
Resolution (Å)	50-3.30 (3.42-3.30)[b]
R_{sym}	15.0 (55.1)
$I/\sigma I$	8.3 (1.8)
Completeness (%)	87.6 (89.0)
Redundancy	2.7 (2.7)
No. of unique reflections	31,300
Refinement	
Resolution (Å)	31.54–3.30
No. of reflections	30,833
R_{work}/R_{free}	0.227/0.283
No. of atoms	11,459
Average *B* factors (Å^2)	
Overall	84.7
P domain	82.4
Fab	86.3
Ramachandran (%)	
Outliers	0.00
Favored	93.31
RMS deviations	
Bond lengths (Å)	0.004
Bond angles (°)	0.795

[a] The data set was collected from a single crystal of the 026_P domain-Fab complex (PDB ID 3V7A).
[b] Values in parentheses are for the highest-resolution shell.

Fitting of the crystal structures of the GII.10 P domain and P domain-Fab complex into the GII.10 VLP cryo-EM map was performed manually and guided by previous fitting results of GV.1 P domain dimers into the GV.1 cryo-EM map (63). This approximate alignment was adjusted computationally using the Fit-in-Map function in UCSF Chimera (52) to a cross-correlation coefficient of 0.94 (Fig. 4). Using this method, the X-ray structure of the GII.10 P domain dimer (PDB ID 3ONU) was unambiguously fitted into the corresponding density in the cryo-EM map, except for several loops on the P2 subdomain (Fig. 4C). This is probably due to flexibility in these domains, as the electron density of the P2 subdomain loops was weak and the tips of the P2 domains were less ordered than the S domain and P1 domains in the cryo-EM reconstruction (data not shown). The P domain dimers appeared to be connected to adjacent, icosahedrally related P1 subdomains in the VLP, whereas the P2 subdomains had no such connections (Fig. 4C). When the P domain from the X-ray structure of the P domain-Fab complex was fitted into the A/B dimer subunit of the reconstruction, the 5B18 Fab was located under the neighboring P domain dimer and rested on top of the S domain at the space at the 2-fold axes (Fig. 5A). When the P domain from the X-ray structure of the P domain-Fab complex was instead fitted into the C/C dimer subunit, the 5B18 Fab made contact with a neighboring P domain dimer and clashed with a star-like protrusion on the S domain at the space at the 5-fold axes (Fig. 5B). Essentially, the epitope of 5B18 overlapped the region of the P1 subdomain that made interactions with icosahedrally related, adjacent P domains in the VLPs when in this "floating P domain" conformation. Based on this modeling, it appeared that the VLP probably could not be saturated with 5B18 antibodies, as this would create a highly unstable structure, as well as additional IgG-IgG steric clashes at the axis spaces. Two possibilities are likely, (i) that 5B18 recognition of intact norovirus particles occurs at select, transiently exposed P domains or (ii) that 5B18 recognition occurs at places where the particle has a defect, where the P domain is exposed because the particle is not appropriately formed.

The 5B18 IgG bound equally well with intact and partially broken GII.10 VLPs. To test whether 5B18 recognition occurs with intact or with broken particles, we assessed the pH behavior of 5B18 recognition, as norovirus VLPs become less stable and appear broken at high pH values (2). We observed that at low and neutral pHs (5.3, 6.3, and 7.3), the GII.10 VLPs were mostly homogenous in size and unbroken, whereas at higher pHs (8.3 and 9.3), the GII.10 VLPs appeared less homogenous in size and partially broken (Fig. 6A). The 5B18 IgG detected GII.10 VLPs at different pH values with nearly identical efficacy, regardless of the fraction of damaged particles (Fig. 6B). At pH 5.3, 6.3, and 8.3, the titer was 512,000, at pH 9.3, the titer was 1,024,000, and at pH 7.3, the titer was 2,048,000 (optical density [OD] cutoff of >0.2) (21).

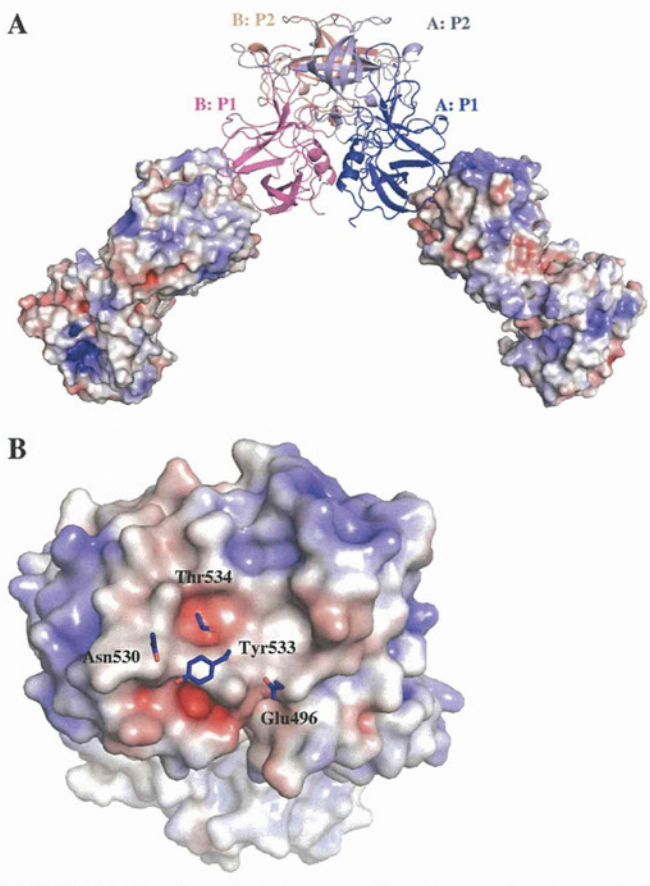

FIG 2 The binding site on the Fab was coordinated by negative charge regions on the Fab. (A) The GII.10 P domain is colored as in Fig. 1. The 5B18 Fab surface is color-coded according to electrostatic potential from red (negative charge) to blue (positive charge). (B) A close-up view of the electrostatic potential on the Fab, showing the four P domain side chain residues on chain A that interacted with the Fab. The P domain side chains bound near the negative charge (red) regions on the Fab.

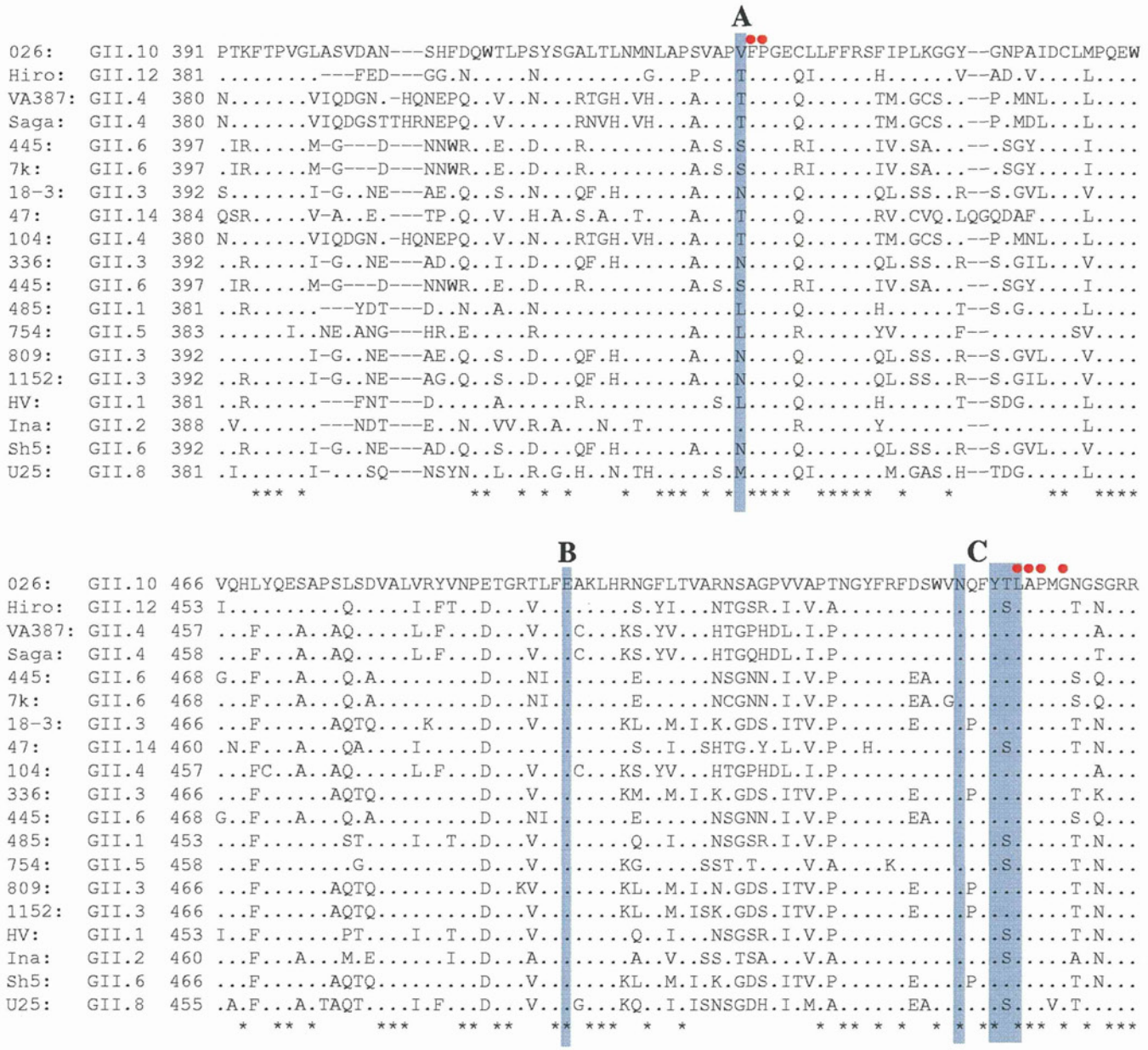

FIG 3 Amino acid alignment of GII capsid sequences indicated that four GII.10 P domain residues involved in binding 5B18 Fab were highly conserved among other GII genotypes. Ten different GII genotypes' capsid sequences were aligned (strain name is followed by genotype), and the GII.10 capsid sequence was used as the consensus (21). The GII.10 P domain residues that interacted with the 5B18 Fab involved three different sites on the P domain, termed A, B, and C. The blue shading shows the six GII.10 P domain residues that interacted with the 5B18 Fab, and from the alignment, four of six residues were highly conserved among other GII genotypes. The red circles show the suspected binding site of MAb14-1 monoclonal antibody (59).

Together, these results suggest that 5B18 appears capable of detecting nominally intact GII.10 VLPs.

Norovirus variability and 5B18 detection. As stated previously, norovirus displays considerable genetic variation. Mapping this variation onto the VLP structure shows that this variation is concentrated on the outer surface of the virion, with buried portions of the P and S domains being much more conserved (Fig. 7). If one were only able to access the outer surface of the VLP, this genetic variation would make pan-recognition extremely difficult. The 5B18 mode of recognition thus provides a mechanism to achieve broad VLP detection by recognizing a conserved surface that is transiently exposed in a dynamic manner. Indeed, the Fab footprint was highly conserved on the GII P domains (Fig. 7C).

DISCUSSION

Human noroviruses are genetically and antigenically distinct, but broad-range monoclonal antibodies capable of detecting multiple norovirus genogroups and genotypes have been described (21, 39, 40, 50, 59, 70). One such antibody, 5B18, is currently in use in a commercial norovirus ELISA detection kit (Denka Seiken, Japan) and was found to bind to numerous GII genotypes but not GI noroviruses (unpublished data). To describe the precise binding

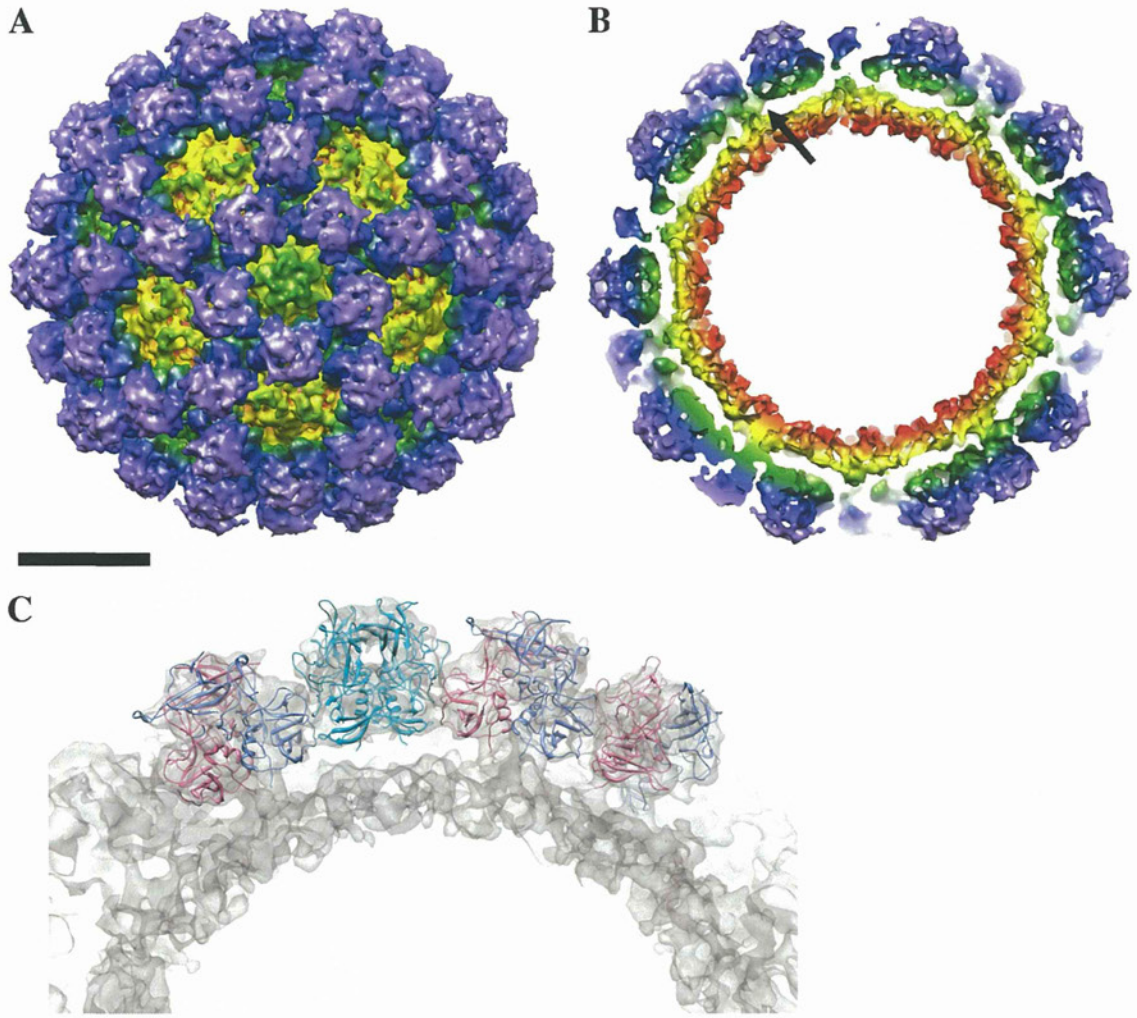

FIG 4 The cryo-EM structure of the GII.10 VLP consisted of an S domain surrounded by 90 P domain dimers. (A) The GII.10 S domain was surface exposed (yellow and yellow to green). The P domain dimers (green to blue and purple) were raised off the S domain by ~15 Å. (B) The inner surface of the S domain is colored red. The S domain was connected to the P domain monomer by a narrow hinge region (single arrow; the other hinges were not labeled for clarity). The scale bar for panels A and B indicates 100 Å. (C) Fitting and modeling of the GII.10 P domain (apo P domain structure) into the A/B dimer subunit (light blue and pink, respectively) and C/C dimer subunit (cyan).

location of 5B18, we determined the X-ray crystal structure of the GII.10 P domain-Fab complex. We also determined the cryo-EM structure of the GII.10 VLPs in an attempt to understand the 5B18 Fab binding interaction in the context of the entire virus particle.

The 5B18 Fab binds to a face of the GII.10 P1 subdomain close to the S domain and not openly exposed at the VLP surface. Six amino acid residues on the P1 subdomain make main chain and side chain interactions with the Fab. Four of these residues are highly conserved among numerous GII norovirus genotypes (Fig. 3). Variation at these residues appears to be tolerated, as the 5B18 antibody detects both GII.4 VLPs, which had Thr433 (instead of Val433), and GII.12 VLPs, which had Thr433 and Ser534 (instead of Val433 and Thr534, respectively). Surprisingly, the 5B18 Fab contact residues are almost identical to those of another broad-range monoclonal antibody, MAb14-1 (Fig. 3) (59). Furthermore, the epitopes of two other broad-range monoclonal antibodies, NV3901 and NV3912, are in this general region (50). The MAb14-1 antibody was shown to bind VLPs from many GII genotypes and several GI genotypes, including a GI.1 genotype, whereas the NV3901 and NV3912 antibodies were found to only bind GI genotypes. Interestingly, the 5B18, MAb14-1, and NV3901/NV3912 antibodies were raised in different mice immunized with different VLPs and their binding sites were all in close proximity on the P1 subdomain (50). Although the precise structural binding details of MAb14-1, NV3901, and NV3912 antibodies have not been described, it suggests that the P1 subdomain was an important antigenic site for GI and GII noroviruses. Moreover, the P1 subdomain likely contained GI and GII cross-reactive epitopes. Superpositioning of published X-ray crystal structures of norovirus P domain (GI.1, GII.4, GII.9, GII.12, and GV.1) onto the GII.10 P domain-Fab complex structure showed that three of six amino acids involved in the 5B18 Fab binding were highly conserved for three norovirus genogroups and that the conformation of their side chains closely resembles those of GII.10 (see Table S2 and Fig. S4 in the supplemental material). Taken together, the results indicate that the 5B18 binding epitope represents an important site for antibody recognition (Fig. 7).

Initially, the X-ray crystal structure of the GI.1 VLP (53) was

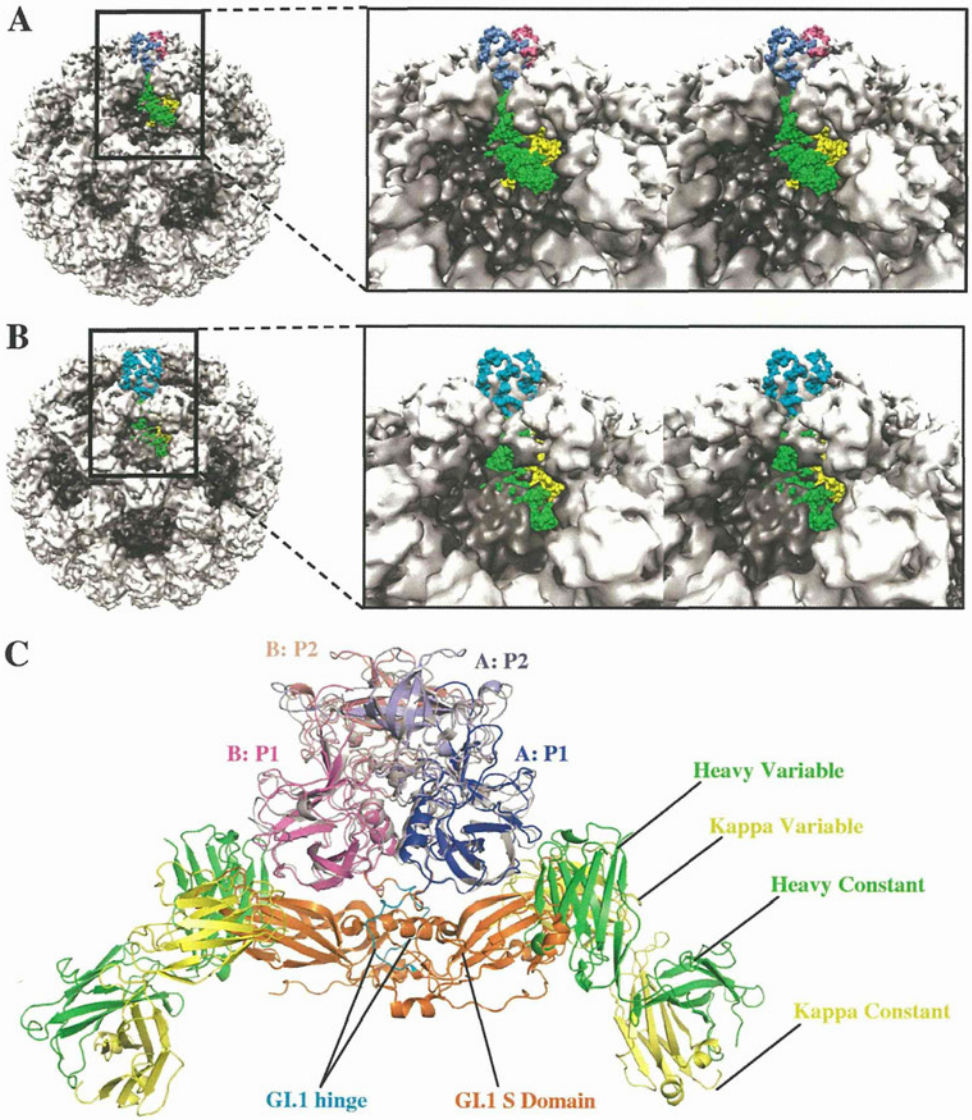

FIG 5 The X-ray crystal structure of the GII.10 P domain-Fab complex fitted into the cryo-EM structure of the GII.10 VLP and the X-ray crystal structure of the GI.1 VLP (PDB ID 1IHM). (A) The P domain (light blue and pink) from the P domain-Fab was fitted into the A/B dimer subunit on the VLP. The boxed region shows a close-up stereoview of the interaction. The Fab appeared to make slight contact with the S domain at the space at the 6-fold axes and was under a neighboring domain. (B) The P domain (cyan) from the P domain-Fab was fitted into the C/C dimer subunit on the VLP. The boxed region shows a close-up stereoview of the interaction. The Fab appeared to make contact with a raised S domain structure at the space at the 5-fold axes and was for the most part hidden under a neighboring domain. (C) The GII.10 P domain (colored as in Fig. 1 and rotated 90° from the views in Fig. 5A and 5B) was highly similar to the GI.1 P domain (light gray), but the Fabs clashed with the GI.1 S domain (orange).

used for fitting the GII.10 P domain-Fab complex and to describe the binding interaction in the context of the entire particle. The P domains of GI.1 and GII.10 matched well (root mean square deviation [RMSD], 1.3 Å), but the 5B18 Fab clashed with the GI.1 S domain (Fig. 5C). Indeed, the P domains in GI.1 VLPs rest on the S domains, and this necessarily placed most of the Fab structure into a position that overlapped the S domain (Fig. 5C). In an attempt to understand the 5B18 antibody interaction in the context of a GII VLP, the cryo-EM structure of the GII.10 VLP was determined to an ~10-Å resolution. Recent cryo-EM studies have shown that GI.1 and GV.1 norovirus capsid structures are strikingly different (30, 67), whereas another study indicated that GI.1 and GII.4 (Grimsby virus) capsids are highly similar (12). The cryo-EM structure of the GII.10 VLPs showed several structural similarities to the GV.1 virion, including a raised P domain, P1-P1 subdomain contacts, and an extended hinge region (see Fig. S6 in the supplemental material). In addition, the GII.10 and GV.1 P domain dimers were rotated ~40° clockwise compared to the orientation of the GI.1 P domain dimer (data not shown). Fitting of the X-ray crystal structure of the GII.10 P domain-Fab complex into the GII.10 VLP structure showed that the P domain could be positioned unambiguously into the P domain density of the EM map; however, this placement resulted in significant overlap between Fab and neighboring P and S domains in the virus particle (Fig. 5). One potential explanation for this result is that the VLPs flexibly expose the P domain to the 5B18 antibody by rotating the

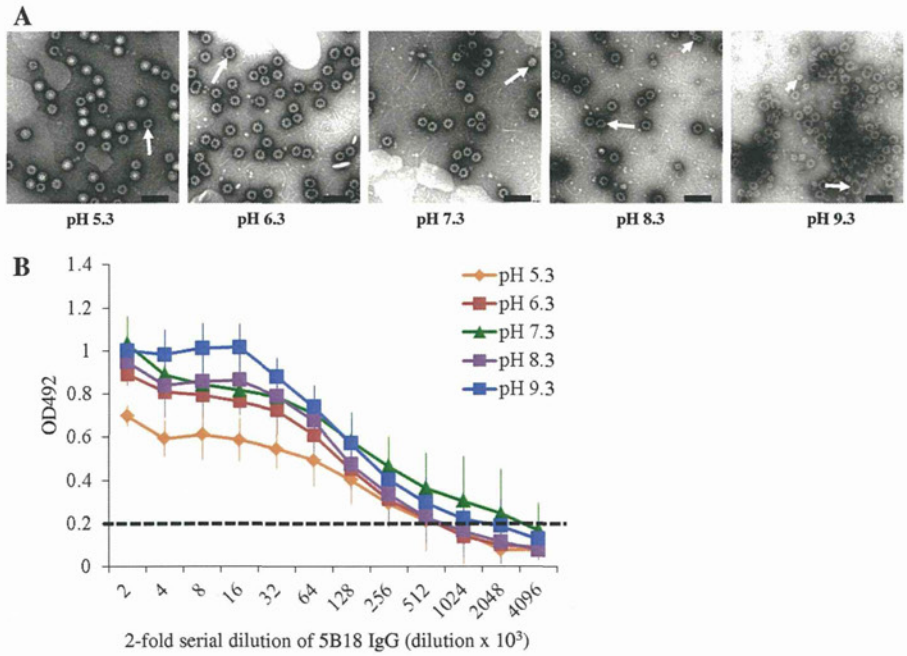

FIG 6 An antibody ELISA was used to determine the binding ability of IgG to GII.10 VLPs. (A) The morphology of the VLPs was examined using EM. At low pHs (from pH 5.3 to 7.3), the majority of the VLPs appeared intact, while above pH 7.3, many of the VLPs appeared broken (long arrows). Small VLPs were also found (short arrows). Scale bar, 100 nm. (B) The same VLPs shown in panel A were used in an ELISA to compare the binding ability of 5B18 IgG. The OD values represent the means of the results for 4 wells; error bars are shown. The OD at 492 nm (OD492) was determined; the dashed line shows the OD492 cutoff of 0.2 (21). The 5B18 IgG detected GII.10 VLPs at different pH values. At pH 7.3, the titer was 2,048,000, while the titers of the other pH values were 2- or 4-fold lower, indicating similar cross-reactivities.

P domains out of the conformation observed in the cryo-EM reconstruction and breaking the P1-P1 domain contacts seen in the VLP. This may be possible since the S domain-P1 subdomain connection in GII noroviruses is particularly long and flexible.

The structural differences between the GI.1 and GII.10 norovirus VLPs do not appear to be a consequence of sequence diversity, since the GI.1 and GII.4 VLP structures are similar and distinct from the GV.1 virion and GII.10 VLP structures. Moreover, the VLP preparation and cryo-EM techniques appear to be essentially the same (54). Two factors that may have affected the particle structures were the insect cell type and the pH of the VLPs. The GI.1 VLPs were expressed in *Spodoptera frugiperda* (Sf9) cells, purified by CsCl ultracentrifugation, and then resuspended in water (pH not described in text) (53, 54), and the GII.10 VLPs were expressed in *Trichopulsia ni* (H5) cells, purified by CsCl ultracentrifugation, and then resuspended in PBS (pH 7.3). We note parenthetically that the cryo-EM structures of hepatitis E virus VLPs expressed in Sf9 and H5 cells are similar, although the processing of the viral protein appeared different (38). Our EM results showed that GII.10 VLPs were intact particles at pH 5.3, 6.3, and 7.3, while another study found that the diameter of norovirus VLPs remained virtually unchanged at pH 3 to 7 but appeared smaller at pH 8 (2). This suggests that the insect cell line and water/PBS (neutral pH) did not affect the overall structure of the VLPs. However, another study has shown that a pH change from 7.6 to 5.0 could cause large structural changes in *Nudaurelia capensis* ω virus VLPs (43, 62). It is possible that these varied conformations do not represent different, stable norovirus structures but are rather all part of a wide spectrum of conformations afforded by the flexible tether between the P and S domains. From previous studies (30), it is clear that this "floating P domain" conformation is independent of whether the sample is a VLP or infectious virion. Since this extended conformation is now observed in rabbit hemorrhagic disease virus (also a calicivirus, genus *Lagovirus*), it also cannot be dependent upon calicivirus genera. It is possible that the energy differences between the conformations represented by these viruses is relatively small and that subtle protein-protein interaction differences favor one conformation under particular conditions. It would be particularly interesting to examine the conformations of these viruses under a broad range of conditions that mimic the expected environments during the viral life cycle. Such changes in virion structure have been observed with numerous other viruses (3, 9, 46, 64, 71). In the case of GV.1 norovirus, where there is an animal model (69) and infectious clone (66), it would also be important to determine what role this flexible tether region has in the replication of the virions and pathology of the disease.

It is important to note that the observed ELISA binding of 5B18 IgG may not occur with intact VLPs. It is possible that denatured or partially broken VLPs or the presence of contaminating GII.10 VP1 was responsible for the binding observed in the ELISA (19, 20, 24). However, it is known that high pH (8.3 or above), partially breaks or denatures norovirus VLPs (2). Despite this pH dependence, the titer remained almost identical, especially in the comparison between pHs 7.3 to 9.3 (Fig. 6), suggesting that only intact or structurally stable virions are being detected. Moreover, the 5B18 antibody could detect GII.10 VLPs that were bound to the plates via histo-blood group antigens, which required a dimeric interaction (22; also unpublished data). Finally three other antibodies, MAb14-1 and NV3901/NV3912, which bound in close

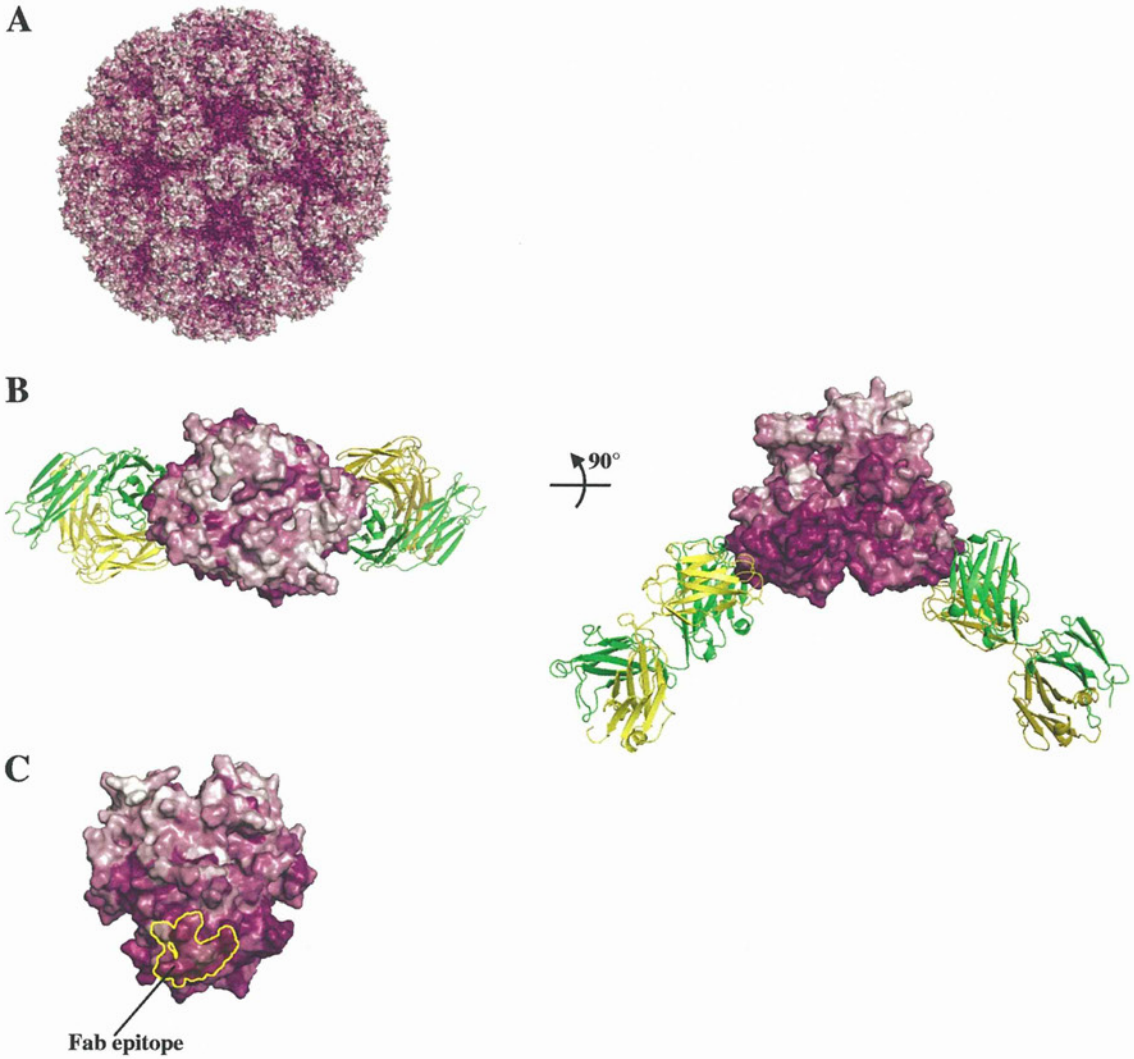

FIG 7 Surface representations of GII amino acid conservation. Noroviruses are genetically and antigenically distinct, with the S domain being more conserved than the P domain. (A) The GII amino acid variability was mapped onto the model of the GII.10 VLP (GI.1 S domain and GII.10 P domain). Amino acid conservation ranges are color-coded from deep purple (highly conserved) to white (highly variable). (B) The amino acid variability was mapped onto the GII.10 P domain apo structure (3ONU) with the 5B18 Fab bound. The top of the P domain was highly variable (left side), while the bottom half of the P domain was more conserved (right side). (C) The Fab binding footprint was mapped onto the P domain (yellow line). The footprint was at a highly conserved area on the wall of the P domain (inside the particle).

proximity to the 5B18 were all shown to detect VLPs (50, 59). These data therefore favor a model in which apparently intact norovirus capsids can indeed bind the 5B18 antibody (and other antibodies) despite significant steric clashes with the VLP structure.

Viruses often use remarkable conformational changes in their envelope or capsid structures to protect their genetic material by waiting for the proper cellular trigger to release their genome into the host cell. For example, the hemagglutinin spike in influenza undergoes a drastic pH-dependent conformational change in the endosome that initiates membrane fusion (8, 68). Similarly large pH-dependent changes have been observed with the enveloped flaviviruses (31, 32, 47) and alphaviruses (36, 45). Such changes due to environmental cues can expose or hide antigenic sites (e.g., see references 41, 45, and 47). Viruses can also receive cues via interactions with cellular receptors, as is the case with human rhinovirus (25, 26, 48). Viruses also undergo small, dynamic structural changes, "breathing" (6, 35, 37, 56), that are probably a prelude to the far larger conformational changes that occur during uncoating. These dynamic motions can transiently expose more-conserved antigenic sites that can be leveraged in designing vaccines (29, 37). However, the fact that these norovirus antibodies are recognizing deeply occluded portions of the P1 domain in apparently intact virions represents a different kind of viral dynamic: for this recognition to occur, the P domains must be capable of extremely large conformational changes without any obvious environmental cue. Such recognition would probably involve just one or a few P domains of a VLP being recognized by antibody 5B18; indeed, images of VLPs after incubation with an excess of antibody 5B18 for 1 h at 37°C (the same incubation used in the ELISA) shows them to be intact, with bound IgG difficult to detect (see Fig. S7 in the supplemental material).

Other antibodies have recently been described that bind to occluded sites on virions. With West Nile virus, the fusion loop-specific antibody E53 recognizes an epitope that should be inaccessible on mature virions. However, this antibody could neutralize mature West Nile virus in a time- and temperature-dependent manner, indicating a role of virus "breathing" or conformational dynamics in antibody recognition (17). With HIV-1, broadly neutralizing antibodies against the membrane-proximal external region of the virus do not appear to recognize the native viral spike (11, 58), again implicating conformational rearrangements to permit antibody recognition. These studies, along with the present study on norovirus recognition by 5B18, suggest substantial flexibility in certain virus particles as being important biologically for antibody-mediated recognition.

In summary, we have shown that a broadly reactive monoclonal antibody binds to an occluded site on the GII.10 P1 subdomain. The binding site was in close proximity to other monoclonal antibody binding sites, suggesting that the site contained an immunodominant region. We also found that the GII.10 VLP structure was more closely related to a GV.1 virion structure than to a GI.1 VLP structure and has marked flexibility in the P domains. These studies suggest that the P domain of noroviruses is capable of adopting variable conformations with respect to the S domain. Despite the vaunted diversity of noroviruses, especially on the exposed outer surface of the virion, one mechanism to achieve near pan-recognition by antibody may be to target a highly conserved domain interface that is dynamically exposed to the environment.

ACKNOWLEDGMENTS

We thank J. Stuckey for assistance with figures and members of the Structural Biology Section at the NIH Vaccine Research Center for help with Fab preparation and comments on the manuscript, K. Nagayama for generous help and insightful discussions, and M. Kataoka for assistance with electron microscopy.

G.S.H. and P.D.K. conceived the project; G.S.H. performed X-ray crystallography and biochemical assays with assistance from J.S.M., S.-Y.P., and P.D.K.; D.W.T. determined the cryo-EM structure with assistance from K.M.; M.Y., F.G., M.M., and K.K. provided the 5B18 IgG; I.G. mapped sequence conservation onto the GII.10 VLP; and G.S.H., D.W.T., J.S.M., T.J.S., I.G., J.R.H.T., K.M., and P.D.K. analyzed the data and wrote the paper, on which all authors commented.

Support for this work was provided by the Intramural Research Program of the National Institutes of Health (NIAID [P.D.K.]), USA, and by a Grant-in-Aid for Scientific Research, grants from the Ministry of Health, Labor, and Welfare of Japan, and a grant from the National Institute of Natural Sciences (NINS), Japan (K.M.). D.W.T is an NSF Graduate Research Fellow and performed this work in Japan as a JSPS/NSF East Asia and Pacific Summer Institute Fellow. Use of Sector 22 (Southeast Region Collaborative Access team) at the Advanced Photon Source was supported by the U.S. Department of Energy, Basic Energy Sciences, Office of Science, under contract no. W-31-109-Eng-38.

REFERENCES

1. **Adams PD, et al.** 2010. PHENIX: a comprehensive Python-based system for macromolecular structure solution. Acta Crystallogr. D. Biol. Crystallogr. **66**(Pt 2):213–221.
2. **Ausar SF, Foubert TR, Hudson MH, Vedvick TS, Middaugh CR.** 2006. Conformational stability and disassembly of Norwalk virus-like particles. Effect of pH and temperature. J. Biol. Chem. **281**:19478–19488.
3. **Belnap DM, et al.** 2000. Molecular tectonic model of virus structural transitions: the putative cell entry states of poliovirus. J. Virol. **74**:1342–1354.
4. **Bhella D, Gatherer D, Chaudhry Y, Pink R, Goodfellow IG.** 2008. Structural insights into calicivirus attachment and uncoating. J. Virol. **82**:8051–8058.
5. **Bhella D, Goodfellow IG.** 2011. The cryo-electron microscopy structure of feline calicivirus bound to junctional adhesion molecule A at 9-angstrom resolution reveals receptor-induced flexibility and two distinct conformational changes in the capsid protein VP1. J. Virol. **85**: 11381–11390.
6. **Bothner B, Dong XF, Bibbs L, Johnson JE, Siuzdak G.** 1998. Evidence of viral capsid dynamics using limited proteolysis and mass spectrometry. J. Biol. Chem. **273**:673–676.
7. **Bu W, et al.** 2008. Structural basis for the receptor binding specificity of Norwalk virus. J. Virol. **82**:5340–5347.
8. **Bullough PA, Hughson FM, Skehel JJ, Wiley DC.** 1994. Structure of influenza haemagglutinin at the pH of membrane fusion. Nature **371**: 37–43.
9. **Canady MA, Tihova M, Hanzlik TN, Johnson JE, Yeager M.** 2000. Large conformational changes in the maturation of a simple RNA virus, nudaurelia capensis omega virus (NomegaV). J. Mol. Biol. **299**:573–584.
10. **Cao S, et al.** 2007. Structural basis for the recognition of blood group trisaccharides by norovirus. J. Virol. **81**:5949–5957.
11. **Chakrabarti BK, et al.** 2011. Direct antibody access to the HIV-1 membrane-proximal external region positively correlates with neutralization sensitivity. J. Virol. **85**:8217–8226.
12. **Chen R, et al.** 2004. Inter- and intragenus structural variations in caliciviruses and their functional implications. J. Virol. **78**:6469–6479.
13. **Choi JM, Hutson AM, Estes MK, Prasad BV.** 2008. Atomic resolution structural characterization of recognition of histo-blood group antigens by Norwalk virus. Proc. Natl. Acad. Sci. U. S. A. **105**:9175–9180.
14. **Collaborative Computational Project N.** 1994. The CCP4 suite: programs for protein crystallography. Acta Crystallogr. D. Biol. Crystallogr. **50**:760–763.
15. **de Bruin E, Duizer E, Vennema H, Koopmans MP.** 2006. Diagnosis of Norovirus outbreaks by commercial ELISA or RT-PCR. J. Virol. Methods **137**:259–264.
16. **Dolinsky TJ, Nielsen JE, McCammon JA, Baker NA.** 2004. PDB2PQR: an automated pipeline for the setup of Poisson-Boltzmann electrostatics calculations. Nucleic Acids Res. **32**:W665–W667.
17. **Dowd KA, Jost CA, Durbin AP, Whitehead SS, Pierson TC.** 2011. A dynamic landscape for antibody binding modulates antibody-mediated neutralization of West Nile virus. PLoS Pathog. **7**:e1002111.
18. **Emsley P, Lohkamp B, Scott WG, Cowtan K.** 2010. Features and development of COOT. Acta Crystallogr. D. Biol. Crystallogr. **66**:486–501.
19. **Graham DY, et al.** 1994. Norwalk virus infection of volunteers: new insights based on improved assays. J. Infect. Dis. **170**:34–43.
20. **Greenberg HB, et al.** 1981. Proteins of Norwalk virus. J. Virol. **37**:994–999.
21. **Hansman GS, et al.** 2006. Genetic and antigenic diversity among noroviruses. J. Gen. Virol. **87**:909–919.
22. **Hansman GS, et al.** 2011. Crystal structures of GII.10 and GII.12 norovirus protruding domains in complex with histo-blood group antigens reveal details for a potential site of vulnerability. J. Virol. **85**:6687–6701.
23. **Hansman GS, et al.** 2004. Detection of norovirus and sapovirus infection among children with gastroenteritis in Ho Chi Minh City, Vietnam. Arch. Virol. **149**:1673–1688.
24. **Hardy ME, White LJ, Ball JM, Estes MK.** 1995. Specific proteolytic cleavage of recombinant Norwalk virus capsid protein. J. Virol. **69**:1693–1698.
25. **Hewat EA, Blaas D.** 2004. Cryoelectron microscopy analysis of the structural changes associated with human rhinovirus type 14 uncoating. J. Virol. **78**:2935–2942.
26. **Hoover-Litty H, Greve JM.** 1993. Formation of rhinovirus-soluble ICAM-1 complexes and conformational changes in the virion. J. Virol. **67**:390–397.
27. **Jiang X, Wang M, Graham DY, Estes MK.** 1992. Expression, self-assembly, and antigenicity of the Norwalk virus capsid protein. J. Virol. **66**:6527–6532.
28. **Kamata K, et al.** 2005. Expression and antigenicity of virus-like particles of norovirus and their application for detection of noroviruses in stool samples. J. Med. Virol. **76**:129–136.
29. **Katpally U, Fu T, Freed DC, Casimiro DR, Smith TJ.** 2009. Antibodies to the buried N-terminus of rhinovirus VP4 exhibit cross-serotypic neutralization. J. Virol. **83**:7040–7048.

30. **Katpally U, et al.** 2010. High-resolution cryo-electron microscopy structures of murine norovirus 1 and rabbit hemorrhagic disease virus reveal marked flexibility in the receptor binding domains. J. Virol. **84**:5836–5841.
31. **Kaufmann B, et al.** 2009. Capturing a flavivirus pre-fusion intermediate. PLoS Pathog. **5**:e1000672.
32. **Kaufmann B, et al.** 2006. West Nile virus in complex with the Fab fragment of a neutralizing monoclonal antibody. Proc. Natl. Acad. Sci. U. S. A. **103**:12400–12404.
33. **Krissinel E, Henrick K.** 2007. Inference of macromolecular assemblies from crystalline state. J. Mol. Biol. **372**:774–797.
34. **Kwong PD, et al.** 1999. Probability analysis of variational crystallization and its application to gp120, the exterior envelope glycoprotein of type 1 human immunodeficiency virus (HIV-1). J. Biol. Chem. **274**:4115–4123.
35. **Lewis JK, Bothner B, Smith TJ, Siuzdak G.** 1998. Antiviral agent blocks breathing of the common cold virus. Proc. Natl. Acad. Sci. U. S. A. **95**: 6774–6778.
36. **Li L, Jose J, Xiang Y, Kuhn RJ, Rossmann MG.** 2010. Structural changes of envelope proteins during alphavirus fusion. Nature **468**:705–708.
37. **Li Q, Yafal AG, Lee YMH, Hogle J, Chow M.** 1994. Poliovirus neutralization by antibodies to internal epitopes of VP4 and VP1 results from reversible exposure of the sequences at physiological temperatures. J. Virol. **68**:3965–3970.
38. **Li TC, et al.** 2005. Essential elements of the capsid protein for self-assembly into empty virus-like particles of hepatitis E virus. J. Virol. **79**: 12999–13006.
39. **Li X, Zhou R, Tian X, Li H, Zhou Z.** 2010. Characterization of a cross-reactive monoclonal antibody against Norovirus genogroups I, II, III and V. Virus Res. **151**:142–147.
40. **Lochridge VP, Jutila KL, Graff JW, Hardy ME.** 2005. Epitopes in the P2 domain of norovirus VP1 recognized by monoclonal antibodies that block cell interactions. J. Gen. Virol. **86**:2799–2806.
41. **Lok S-M, et al.** 2008. Binding of a neutralizing antibody to dengue virus alters the arrangement of surface glycoproteins. Nat. Struct. Mol. Biol. **15**:312–317.
42. **Majeed S, et al.** 2003. Enhancing protein crystallization through precipitant synergy. Structure **11**:1061–1070.
43. **Matsui T, Lander G, Johnson JE.** 2009. Characterization of large conformational changes and autoproteolysis in the maturation of a T=4 virus capsid. J. Virol. **83**:1126–1134.
44. **McCoy AJ, et al.** 2007. Phaser crystallographic software. J. Appl. Crystallogr. **40**:658–674.
45. **Meyer WJ, Gidwitz S, Ayers VK, Schoepp RJ, Johnston RE.** 1992. Conformational alteration of Sindbis virion glycoproteins induced by heat, reducing agents, or low pH. J. Virol. **66**:3504–3513.
46. **Miao Y, Johnson JE, Ortoleva PJ.** 2010. All-atom multiscale simulation of cowpea chlorotic mottle virus capsid swelling. J. Phys. Chem. B. **114**: 11181–11195.
47. **Modis Y, Ogata S, Clements D, Harrison SC.** 2004. Structure of the dengue virus envelope protein after membrane fusion. Nature **427**:313–319.
48. **Olson NH, et al.** 1993. Structure of a human rhinovirus complexed with its receptor molecule. Proc. Natl. Acad. Sci. U. S. A. **90**:507–511.
49. **Otwinowski Z, Minor W.** 1997. Processing of X-ray diffraction data collected in oscillation mode. Methods Enzymol. **276**:307–326.
50. **Parker TD, Kitamoto N, Tanaka T, Hutson AM, Estes MK.** 2005. Identification of genogroup I and genogroup II broadly reactive epitopes on the norovirus capsid. J. Virol. **79**:7402–7409.
51. **Pei J, Grishin NV.** 2001. AL2CO: calculation of positional conservation in a protein sequence alignment. Bioinformatics **17**:700–712.
52. **Pettersen EF, et al.** 2004. UCSF Chimera—a visualization system for exploratory research and analysis. J. Comput. Chem. **25**:1605–1612.
53. **Prasad BV, et al.** 1999. X-ray crystallographic structure of the Norwalk virus capsid. Science **286**:287–290.
54. **Prasad BV, Rothnagel R, Jiang X, Estes MK.** 1994. Three-dimensional structure of baculovirus-expressed Norwalk virus capsids. J. Virol. **68**: 5117–5125.
55. **Rabenau HF, et al.** 2003. Laboratory diagnosis of norovirus: which method is the best? Intervirology **46**:232–238.
56. **Reisdorph N, et al.** 2003. Human rhinovirus capsid dynamics is controlled by canyon flexibility. Virology **314**:34–44.
57. **Richards AF, et al.** 2003. Evaluation of a commercial ELISA for detecting Norwalk-like virus antigen in faeces. J. Clin. Virol. **26**:109–115.
58. **Ruprecht CR, et al.** 2011. MPER-specific antibodies induce gp120 shedding and irreversibly neutralize HIV-1. J. Exp. Med. **208**:439–454.
59. **Shiota T, et al.** 2007. Characterization of a broadly reactive monoclonal antibody against norovirus genogroups I and II: recognition of a novel conformational epitope. J. Virol. **81**:12298–12306.
60. **Tan M, Hegde RS, Jiang X.** 2004. The P domain of norovirus capsid protein forms dimer and binds to histo-blood group antigen receptors. J. Virol. **78**:6233–6242.
61. **Tang G, et al.** 2007. EMAN2: an extensible image processing suite for electron microscopy. J. Struct. Biol. **157**:38–46.
62. **Tang J, et al.** 2009. Dynamics and stability in maturation of a T=4 virus. J. Mol. Biol. **392**:803–812.
63. **Taube S, et al.** 2010. High-resolution X-ray structure and functional analysis of the murine norovirus 1 capsid protein protruding domain. J. Virol. **84**:5695–5705.
64. **Trus BL, et al.** 1996. The herpes simplex virus procapsid: structure, conformational changes upon maturation, and roles of the triplex proteins VP19c and VP23 in assembly. J. Mol. Biol. **263**:447–462.
65. **van Heel M, Harauz G, Orlova EV, Schmidt R, Schatz M.** 1996. A new generation of the IMAGIC image processing system. J. Struct. Biol. **116**: 17–24.
66. **Ward VK, et al.** 2007. Recovery of infectious murine norovirus using pol II-driven expression of full-length cDNA. Proc. Natl. Acad. Sci. U. S. A. **104**:11050–11055.
67. **Widdowson M-A, et al.** 2005. Detection of serum antibodies to bovine norovirus in veterinarians and the general population in the Netherlands. J. Med. Virol. **76**:119–128.
68. **Wilson IA, Skehel JJ, Wiley DC.** 1981. Structure of the haemagglutinin membrane glycoprotein of influenza virus at 3Å resolution. Nature **289**: 366–373.
69. **Wobus CE, Thackray LB, Virgin HW.** 2006. Murine norovirus: a model system to study norovirus biology and pathogenesis. J. Virol. **80**:5104–5112.
70. **Yoda T, et al.** 2003. Precise characterization of norovirus (Norwalk-like virus)-specific monoclonal antibodies with broad reactivity. J. Clin. Microbiol. **41**:2367–2371.
71. **Yu IM, et al.** 2008. Structure of the immature dengue virus at low pH primes proteolytic maturation. Science **319**:1834–1837.
72. **Zheng DP, et al.** 2006. Norovirus classification and proposed strain nomenclature. Virology **346**:312–323.

OPEN ACCESS Freely available online

PLOS | ONE

VCP Is an Integral Component of a Novel Feedback Mechanism that Controls Intracellular Localization of Catalase and H_2O_2 Levels

Katsuhiro Murakami[1], Yuzuru Ichinohe[1], Masaaki Koike[1], Norio Sasaoka[1], Shun-ichiro Iemura[2], Tohru Natsume[2], Akira Kakizuka[1]*

1 Laboratory of Functional Biology, Kyoto University Graduate School of Biostudies, Sakyo-ku, Kyoto, Japan, **2** National Institutes of Advanced Industrial Science and Technology, Biological Information Research Center (JBIRC), Kohtoh-ku, Tokyo, Japan

Abstract

Catalase is a key antioxidant enzyme that catalyzes the decomposition of hydrogen peroxide (H_2O_2) to water and oxygen, and it appears to shuttle between the cytoplasm and peroxisome via unknown mechanisms. Valosin-containing protein (VCP) belongs to the AAA class of ATPases and is involved in diverse cellular functions, e.g. cell cycle and protein degradation, etc. Here we show that VCP and PEX19, a protein essential for peroxisome biogenesis, interact with each other. Knockdown of either VCP or PEX19 resulted in a predominantly cytoplasmic redistribution of catalase, and loss of VCP ATPase activity also increased its cytoplasmic redistribution. Moreover, VCP knockdown decreased intracellular ROS levels in normal and H_2O_2-treated cells, and an oxidation-resistant VCP impaired the ROS-induced cytoplasmic redistribution of catalase. These observations reveal a novel feedback mechanism, in which VCP can sense H_2O_2 levels, and regulates them by controlling the localization of catalase.

Citation: Murakami K, Ichinohe Y, Koike M, Sasaoka N, Iemura S-i, et al. (2013) VCP Is an Integral Component of a Novel Feedback Mechanism that Controls Intracellular Localization of Catalase and H_2O_2 Levels. PLoS ONE 8(2): e56012. doi:10.1371/journal.pone.0056012

Editor: Junji Yodoi, Institute for Virus Research, Laboratory of Infection and Prevention, Japan

Received October 2, 2012; **Accepted** January 4, 2013; **Published** February 14, 2013

Funding: This work was supported in part by research grants from Solution Oriented Research for Science and Technology (SORST) of Japan Science and Technology Agency (JST), the Ministry of Education, Culture, Sports, Science, and Technology of Japan, and the Ministry of Health, Labour, and Welfare of Japan. The funders had no role in study design, data collection and analysis, decision to publish, or preparation of the manuscript.

Competing Interests: The authors have declared that no competing interests exist.

* E-mail: kakizuka@lif.kyoto-u.ac.jp

Introduction

Reactive oxygen species (ROS), e.g. superoxide radicals, hydrogen peroxide, etc., are natural byproducts of the aerobic metabolism of foods, and they have been shown to play important roles in several physiological functions, e.g. transcriptional regulation, mitogen signaling, integrin signaling, Wnt signaling, etc. (see refs in [1–3]). On the other hand, ROS are also produced by UV and X-ray exposure or inflamation, and excess ROS can damage cellular functions by oxidizing proteins, lipids, and DNA, leading to cell aging as well as cancer (see refs in [4]). Among ROS, the superoxide radical is enzymatically converted by superoxide dismutases (SODs) to hydrogen peroxide (H_2O_2), which, in turn, is converted by catalase or peroxidases to H_2O and O_2. Mammalian cells typically possess three SODs, several peroxidases, and one catalase. Among these ROS-scavenging enzymes, only catalase resides in peroxisomes. In certain conditions, such as aging, catalase also resides in the cytoplasm [5], which is believed to be due to its weak peroxisome-targeting signal (PTS). Two types of PTS, PTS1 and PTS2, are known [6]. Typically, PTS1 consists of three sequential amino acids, SKL, and it is present in peroxisome-localized proteins such as peroxisomal Acyl-CoA thioesterase, PTE1. Catalase has a unique PTS1, consisting of four sequential amino acids, KANL. Both PTS1s are recognized by PEX5 (Peroxisome biogenesis factor 5); however, PEX5 binds to SKL more strongly than to KANL [7], and thus it is believed that PEX5 can transfer SKL-containing proteins more effectively than catalase to peroxisomes. In aged cells, cellular levels of ROS increase, and it is thought that such ROS may weaken PEX5 functions, with transport of catalase to peroxisomes being preferentially compromised, as opposed to transport of SKL-possessing proteins [8]. However, no clear evidence has been provided supporting this speculation.

VCP belongs to the AAA class of ATPases and has been shown to function in many cellular events, including ERAD (endoplasmic reticulum-associated degradation), cell cycle control, membrane fusion, maintenance of Golgi apparatus, protein aggregate formation and clearance, etc. (see refs in [9]). VCP has also been shown to play important roles in several human neurodegenerative disorders [10–12]. We have shown that VCP is modified post-translationally at 60 amino acids, at least, including 18 serines, 14 threonines, 6 tyrosines, and 22 lysines [13]. To investigate the role of post-transcriptional modifications of VCP, we created several modification-mimic forms of VCP, and characterized them [12–14]. These analyses have revealed novel VCP functions and have led us to speculate that VCP may have unidentified functions. In this study, we report a novel VCP function in regulation of intracellular H_2O_2 levels via the control of catalase localization.

Materials and Methods

Antibodies

The following antibodies were purchased: anti-actin (Chemicon), anti-catalase (Calbiochem), anti-PTE1 (ACOT8) (Santa Cruz), anti-FLAG M2 (Sigma), anti-PMP70 (Zymed), anti-HA (Santa Cruz), and anti-PEX19 (BD PharMingen). The affinity-purified rabbit polyclonal anti-VCP antibody was described previously [15].

Plasmids and siRNAs

The cDNAs for PEX5, PEX19, catalase, and PTS2 signal sequences of ACAA1 (acetyl-CoA acyltransferase 1) were amplified by RT–PCR from total RNA isolated from HeLa cells, and their sequences were confirmed. The VCP cDNAs (wtVCP, VCP[K251A], VCP[K524A] [16]) or PEX5 cDNA was subcloned into pmCherry vector (Clontech). The PEX19 cDNA was subcloned into pCMV-HA vector (Clontech).

The targeting sequences of siRNAs for VCP and PEX5 mRNAs were as follows:

VCP(nc), 5′-CGGGAGAGGCGCGCGCCAT-3′;
VCP(286), 5′-GGTTAATTGTTGATGAAGCCATCAA-3′;
PEX5(192), 5′-CAAGCCTTTGGGAGTAGCTTCTGAA-3′;
PEX5(955), 5′-GACCTTACGTCAGCTACCTATGATA-3′.
Control, 5′-CGGACGCGTCAGGAGCCGGTT-3′.

The siRNAs for PEX19 were purchased from Invitrogen (Stealth Select RNAi, HSS108913 and HSS108914, respectively).

Cell Culture and Cell Lines

HeLa cells and HEK293A cells were grown at 37°C in Dulbecco's modified Eagle's medium supplemented with 10% fetal bovine serum. HeLa cell lines stably expressing organelle-targeted GFPs were created by transfection of organelle-targeted GFP expression vectors, and selected in the presence of 2.5 μg/ml of puromycin (Invivogen). The HEK293A cell line stably expressing GFP-catalase, was also created by similar methods.

Transfection and Immunostaining

Plasmid transfection was carried out using Lipofectamine plus (Invitrogen), and siRNA transfection was carried out using Oligofectamine (Invitrogen) according to the manufacturer's protocol. In co-transfection experiments, cells were transfected with siRNA and plasmid using Lipofectamine 2000 (Invitrogen).

Cells were fixed with 4% formaldehyde for 10 min at room temperature. Fixed cells were permeabilized with 0.5% Triton X-100 in PBS for 10 min at room temperature and blocked with blocking buffer (0.1% bovine serum albumin and 0.1% skim milk in PBS) for 1 h. Cells were then incubated 1 h at room temperature with primary antibodies. Subsequently, cells were treated with Alexa Fluor 488-conjugated secondary antibodies (Invitrogen). To detect PMP70, fixed cells were permeabilized with 25 μg/ml digitonin in PBS for 5 min at room temperature, and cells were processed for immunostaining as describe above.

Subcellular Fractionation and Immunoprecipitation

Cells were fractionated into cytosol, membrane/organelle, and nucleus, using a Subcellular Proteome extraction kit (Calbiochem), according to the manufacturer's protocol. Immunoprecipitation assays were performed as described previously [16]. Briefly, samples were lysed on ice and debris was removed by centrifugation for 30 min at 15,000×g at 4°C. The supernatant was mixed with an anti-HA or anti-FLAG antibody and rotated at 4°C overnight after addition of protein G-Sepharose beads (Amersham Biosciences). After washing of beads, bound proteins were analyzed by Western blot.

Intracellular ROS Detection

Cells were washed twice with HBSS and incubated with 5 μM CM-H_2DCFDA, a ROS-detection reagent (Invitrogen), in HBSS at 37°C for 30 min. Subsequently, cells were washed twice with HBSS and incubated with growth medium at 37°C for 30 min with or without H_2O_2. Then cells were analyzed by FACScan flow cytometer (BD Biosciences) or LSM510 confocal microscopy (Carl Zeiss).

Statistical Analysis

Each experiment was conducted at least three times with consistent results. The gel or blot representative of each experiment is presented in this study. The statistical significance was analyzed using Student's *t* test.

Results

Involvement of VCP in Intracellular Localization of Catalase

In order to visualize organelle in live cells, we generated several HeLa cell sublines in which GFP was expressed as a fusion protein with a peroxisomal (PTS1 or PTS2)-, nuclear (NLS)-, ER (KDEL)-, or mitochondrial (mito)-targeting signal. Among these, we observed clear mislocalization of GFP-PTS1 (namely, GFP-SKL and GFP-KANL) into the cytoplasm when the cells were treated with VCP siRNAs but not a control siRNA. VCP siRNAs perturbed GFP-KANL localization much more severely than GFP-SKL localization (**Fig. 1A and B**). By contrast, VCP siRNAs did not induce clear mislocalization of PTS2-GFP, mito-GFP, GFP-ER, or GFP-NLS (Fig. S1). We observed similar mislocalization of GFP-KANL by expressing ATPase-negative or dominant-negative VCP mutants, e.g. VCP[K251A] and VCP[K524A] [16] (Fig. S2). In addition, treating cells with DBeQ, a VCP inhibitor [17], also induced cytoplasmic localization of GFP-catalase (**Fig. 1C**). These results suggest that the ATPase activity of VCP is necessary for proper localization of catalase.

We then examined the effects of VCP knockdown on intracellular localization of endogenous PTE1 or catalase. In more than 50% of cells treated with VCP siRNAs, endogenous catalase was diffusely observed in the cytoplasm. In contrast, PTE1 localization was not apparently affected by VCP knockdown (**Fig. 1D**). These results were confirmed by cell fractionation experiments. VCP siRNA treatments increased the amounts of catalase but not PTE1 in the cytoplasmic fraction (**Fig. 1E**). Mislocalization of catalase as well as GFP-KANL decreased in cells treated with VCP siRNA together with cycloheximide (Fig. S3), supporting the idea that newly synthesized catalase is transported into peroxisomes with the help of VCP.

Interaction between VCP and PEX19

In order to obtain insights for molecular mechanisms underlying VCP-mediated regulation of catalase localization, we searched for VCP-interacting proteins using an immunoprecipitation method followed by a very sensitive MS/MS analysis [18], and identified PEX19 as a potential VCP-interacting protein. Indeed, we could observe a physical association between VCP and PEX19 via immunoprecipitation and western blotting (**Fig. 2**). This interaction appeared very weak, suggesting the possibility that yet-unknown VCP modification may enhance this interaction. This possibility remained to be clarified.

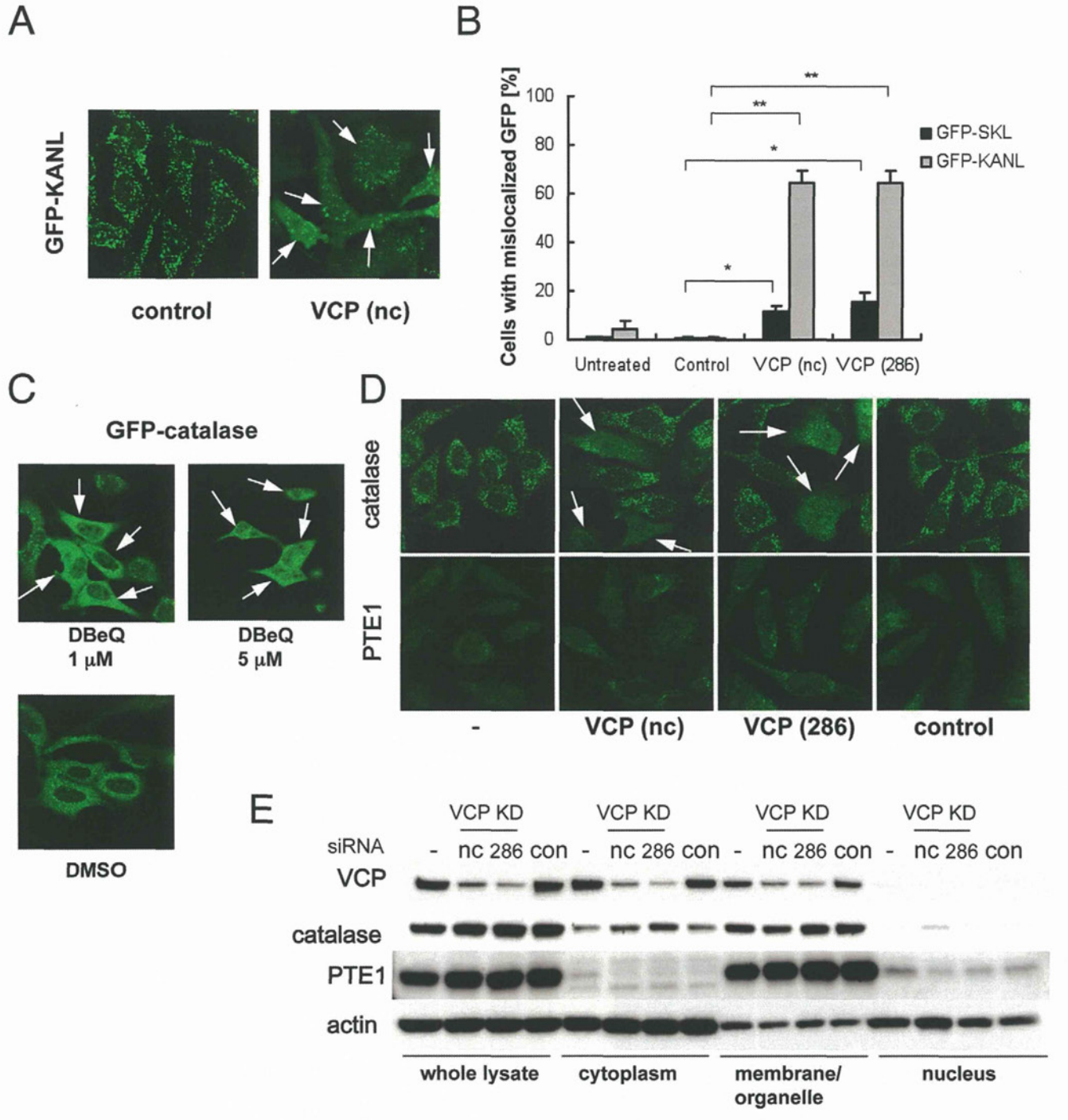

Figure 1. VCP siRNAs induce cytoplasmic localization of catalase. (A) Cytochemical analysis of intracellular localization of GFP-KANL. HeLa cells continuously expressing GFP-KANL were treated with control siRNA (control) or VCP siRNAs (nc and 286). Seventy-two hours later, GFP images were analyzed by confocal microscopy. Arrows indicate cells with cytoplasmic localization of GFP-KANL. (B) Quantification of cytochemical analysis on GFP-KANL in (A) and on GFP-SKL. More than 200 cells were examined in each sample, and the fraction (%) of cells with diffuse GFP signals in the cytoplasm were scored. $^{**}p<0.01$, $^{*}p<0.05$. (C) Fluorescence microscopy analysis of intracellular localization of GFP-catalase. HEK293A cells continuously expressing GFP-catalase were treated with 1 μM or 5 μM DBeQ, a VCP inhibitor [17], or DMSO for 24 hours, and then GFP signals were detected. Arrows indicate cells with cytoplasmic localization of GFP-catalase. (D) Immunocytochemical analysis of intracellular localization of catalase and PTE1. HeLa cells were treated without (−) or with control siRNA (control), or VCP siRNAs (nc and 286). Seventy-two hours later, catalase and PTE1 were detected with anti-catalase and anti-PTE1 antibodies, respectively. Arrows indicate cells with cytoplasmic localization of catalase. (E) Western blot analyses of protein levels of VCP, catalase, and PTE1 in different cell compartments. HeLa cells were treated without (−) or with control siRNA (control) or VCP siRNAs (nc and 286). Seventy-two hours later, cells were fractionated as described in Methods. Fractionated samples equivalent to 7.5 μg total protein of whole cell lysates were separated by SDS-PAGE and analyzed by western blotting using specific antibodies. Actin served as a loading control.

doi:10.1371/journal.pone.0056012.g001

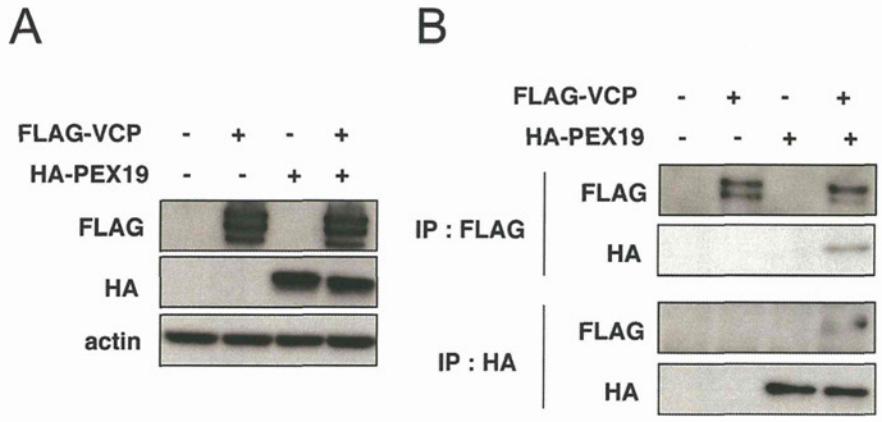

Figure 2. Immunoprecipitation assays to detect physical interactions between VCP and PEX19. (A) HEK293A cells were transfected with expression vectors for FLAG-VCP and HA-PEX19. Twenty-four hours later, cells were harvested and the cell lysates were analyzed by western blots with antibodies indicated in the panels. Actin served as a loading control. (B) The immunoprecipitation was performed on the cell lysates in (A) with an anti-FLAG or anti-HA antibody. The precipitates were analyzed by western blots with antibodies indicated in the panels. See details in **Materials and methods.**
doi:10.1371/journal.pone.0056012.g002

Involvement of PEX19 in Intracellular Localization of Catalase

Given that VCP could potentially make a complex with PEX19 and that VCP knockdown apparently affected the transport of catalase into peroxisomes, PEX19 knockdown could also affect the intracellular localization of catalase. Indeed, PEX19 knockdowns produced virtually identical distributions of intracellular catalase as were observed in VCP knockdowns (**Fig. 3A and B**). Moreover, in PEX19 knockdown cells, PTE1 localization was not apparently affected (**Fig. 3A and B**). PEX19 is reportedly involved in the transport of membrane proteins, such as PMP70 (peroxisome membrane protein 70), to peroxisomes. However, we could not detect any clear mislocalization of endogenous PMP70 in VCP-depleted HeLa cells (Fig. S4).

Consistent with previous reports, PEX5 knockdown induced mislocalization of both catalase and PTE1 (Fig. S5). It is notable that over-expression of PEX5 and VCP could not rectify the mislocalization of GFP-KANL in VCP and PEX5 knockdown cells, respectively (Fig. S6). These results indicate that VCP/PEX19 complexes are required for PEX5 to transport catalase, but not other typical PTS1- or PTS2-possessing proteins, to peroxisomes.

VCP Activity, Catalase Localization, and ROS Levels

We next examined the possibility that VCP-depleted cells have a greater capacity to scavenge H_2O_2 as compared with non-treated cells, due to the presence of catalase in the cytoplasm. This was indeed the case. Basal ROS levels were reduced in cells treated with VCP siRNAs compared to those treated with control siRNAs (**Fig. 4A**). Reduction of ROS levels was more pronounced when cells were treated with H_2O_2 (**Fig. 4A and B**). We have previously shown that the ATPase activity of VCP was inactivated

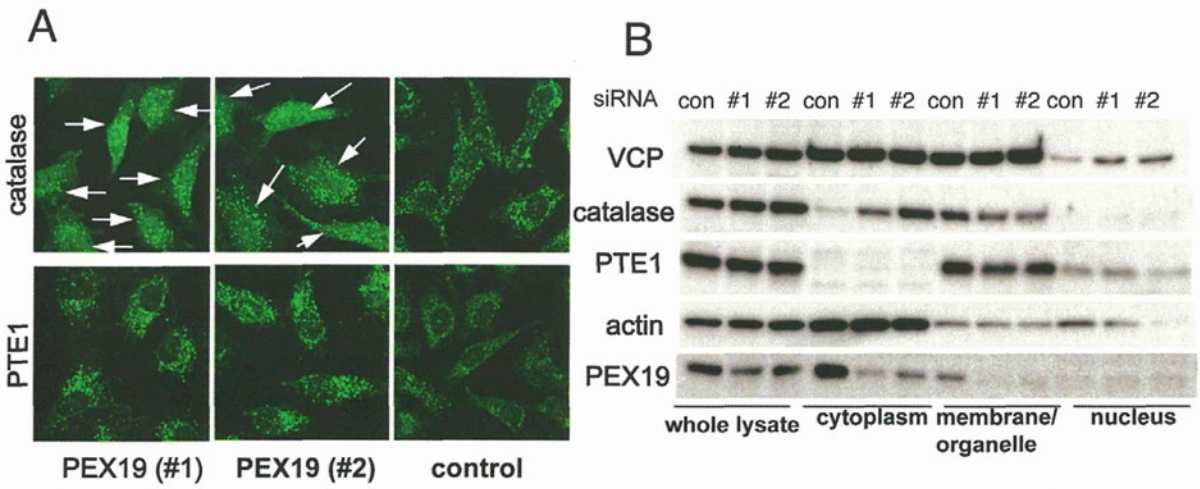

Figure 3. PEX19 siRNAs also induce cytoplasmic localization of catalase. (A) Immunocytochemical analysis of intracellular localization of catalase and PTE1. HeLa cells were treated with control siRNA (control) or PEX19 siRNAs (#1; HSS108913 and #2; HSS108914). Seventy-two hours later, catalase and PTE1 were detected as in (Fig. 1D). Arrows indicate cells with cytoplasmic localization of catalase. (B) Western blot analyses of protein levels of VCP, catalase, PTE1, and PEX19 in different cell compartments. HeLa cells were treated with control siRNA (control) or PEX19 siRNAs (#1; HSS108913 and #2; HSS108914). Seventy-two hours later, cells were analyzed as in (Fig. 1E).
doi:10.1371/journal.pone.0056012.g003

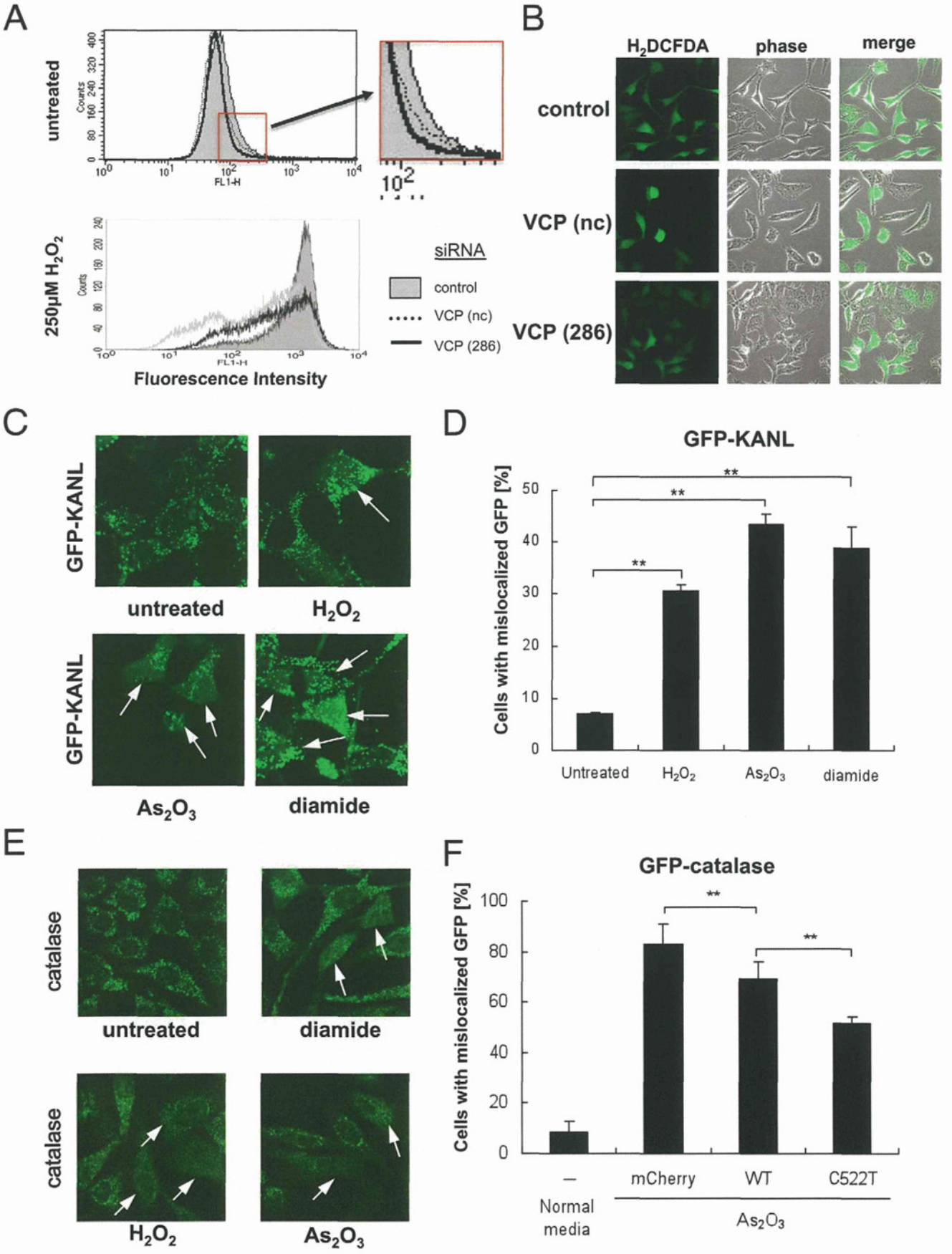
A
untreated
Counts
FL1-H
250μM H_2O_2
Fluorescence Intensity
siRNA
control
VCP (nc)
VCP (286)
B
H_2DCFDA
phase
merge
control
VCP (nc)
VCP (286)
C
GFP-KANL
untreated
H_2O_2
As_2O_3
diamide
D
GFP-KANL
Cells with mislocalized GFP [%]
Untreated
H_2O_2
As_2O_3
diamide
E
catalase
untreated
diamide
H_2O_2
As_2O_3
F
GFP-catalase
Cells with mislocalized GFP [%]
Normal media
mCherry
WT
C522T
As_2O_3

Figure 4. ROS levels and intracellular localization of GFP-KANL and catalase in cells with VCP depletion or overexpression. (A) ROS levels in cells with VCP depletion. HeLa cells were treated with control (control) or VCP (nc and 286) siRNAs. Seventy-two hours later, 5 μM H_2DCFDA was added to the media for 30 min. Then, cells were treated with or without 250 μM H_2O_2 at 37°C for additional 30 min, and analyzed by FACS (see details in **Materials and methods**). (B) Cytochemical analysis of HeLa cells treated with 250 μM H_2O_2. H_2DCFDA fluorescence was analyzed by confocal microscopy as in (A). (C) Cytochemical analysis of intracellular localization of GFP-KANL after treatment of ROS-producing agents. HEK293A cells continuously expressing GFP-KANL were treated with 250 μM H_2O_2, 20 nM As_2O_3, or 250 μM diamide. Twenty-four hours later, GFP images were analyzed by confocal microscopy. Arrows indicate cells with cytoplasmic localization of GFP-KANL. (D) Quantification of cytochemical analysis in (C). More than 200 cells were examined in each sample, and the fraction (%) of cells with diffuse GFP signals in the cytoplasm were scored. $^{**}p<0.01$. (E) Immunocytochemical analysis of intracellular localization of catalase after treatment with ROS-producing agents. HeLa cells were treated with 500 μM H_2O_2, 20 nM As_2O_3, or 250 μM diamide. Twenty-four hours later, catalase was detected with an anti-catalase antibody. Arrows indicate cells with cytoplasmic localization of catalase. (F) Overexpression of VCP[C522T] weakened cytoplasmic localization of catalase by ROS more significantly than that of wild-type VCP. HEK293A cells continuously expressing GFP-catalase were transfected with VCP[C522T]-mCherry (C522T) or wild-type VCP-mCherry (wtVCP), and treated with 20 nM As_2O_3 for 24 hours. More than 200 mCherry-positive cells were examined in each sample, and the fraction (%) of cells with diffuse GFP signals in the cytoplasm were scored. $^{**}p<0.01$.
doi:10.1371/journal.pone.0056012.g004

by oxidation of Cys522 by ROS, such as H_2O_2 [14]. The observation that ATPase activity of VCP is necessary for proper catalase localization to peroxisomes raised the possibility that ROS treatments would also induce redistribution of catalase. We next examined this possibility, and confirmed that all tested ROS-inducing agents (such as H_2O_2, As_2O_3, and diamide) induced cytoplasmic localization of GFP-KANL as well as catalase (**Fig. 4C–E**). We then examined whether VCP[C522T], a VCP mutant with the ROS-sensitive cysteine to threonine substitution [14], had protective effects on redistribution of catalase in cells treated with ROS. Indeed, overexpression of VCP[C522T] significantly inhibited cytoplasmic localization of catalase in cells treated with As_2O_3, compared to overexpressed wild-type VCP (**Fig. 4F**).

Discussion

The results presented in this study, taken together, point to the existence of a novel feedback mechanism: when H_2O_2 levels increase, VCP ATPase is inactivated by Cys522 oxidation, which in turn keeps catalase in the cytoplasm, leading to reduced H_2O_2 levels. After H_2O_2 levels are reduced, glutathione as well as thioredoxine levels would recover, which would then restore VCP ATPase activity, leading to catalase transport into peroxisomes. This VCP-mediated system has the great merit of specifically changing the localization of catalase without affecting the localization of other peroxisome proteins.

In *S. cerevisiae*, Cys522 is not conserved in Cdc48p, a VCP homologue [14]. In what appears to be an evolutionary alternative design, *S. cerevisiae* possesses two catalases, one of which resides in peroxisomes and the other in the cytoplasm [19,20]. *C. elegans* also possesses two catalases, one in peroxisomes and the other in the cytoplasm [21]. These lines of evidence strongly indicate that for living organisms catalase is needed in both peroxisomes and the cytoplasm. In mammals, a certain level of ROS, namely H_2O_2, is utilized in several physiological conditions, and, therefore the continuous presence of catalase in the cytoplasm might not be favorable. On the other hand, when mammalian cells meet conditions with a large amount of H_2O_2 in the cytoplasm, catalase would more effectively degrade and reduce H_2O_2 by accumulating in the cytoplasm. Thus, mammals have developed an integrated system to utilize one catalase rather than to have two differently localized catalases.

Supporting Information

Figure S1 Fluorescence microscopy analysis of intracellular localization of PTS2-GFP, mito-GFP, GFP-ER, and GFP-NLS. (A) Schematic drawings of GFP-fused proteins. (B) HeLa cells were treated with control siRNA (control) or VCP siRNAs (nc and 286). Seventy-two hours later, GFP signals were detected.
(TIFF)

Figure S2 Fluorescence microscopy analysis of intracellular localization of GFP-KANL in the presence of ATPase activity-defective mutant VCPs. (A) HEK293A cells continuously expressing GFP-KANL were transfected with an expression vectors for mCherry or VCP (wtVCP, VCP[K251A] [15], or VCP[K524A] [15])-mCherry. Forty-eight hours later, GFP signals were detected. (B) Quantification of fluorescence microscopy of GFP-KANL in (A). More than 200 mCherry-positive cells were examined in each sample, and the fraction (%) of cells with diffuse GFP signals in the cytoplasm were scored. $^{**}p<0.01$, $^{*}p<0.05$.
(TIFF)

Figure S3 Immunocytochemical and fluorescence microscopy analyses of intracellular localization of catalase and GFP-KANL. (A) HeLa cells were treated with control siRNA (control) or VCP siRNA (286) for 72 hours, and treated with or without cyclohexamide (CHX) (5 μg/ml) for additional 24 hours. Then catalase was detected with anti-catalase antibody. (B) HeLa cells continuously expressing GFP-KANL were treated with VCP siRNA (286). Cells were treated with or without 5 μg/ml of CHX from 48 (24 h) or 24 (48 h) to 72 hours after siRNA treatment. Then, GFP signals were detected.
(TIFF)

Figure S4 Immunocytochemical analysis of intracellular localization of PMP70. HeLa cells were treated without (−) or with control siRNA (control), or VCP siRNAs (nc and 286). Seventy-two hours later, PMP70 was detected with an anti-PMP70 antibody. Note that VCP protein levels decreased by VCP siRNA treatments, as shown in Fig. 1E
(TIFF)

Figure S5 Immunocytochemical analysis of intracellular localization of catalase and PTE1. HeLa cells were treated with control siRNA (control) or PEX5 siRNAs (192 and 955). Seventy-two hours later, catalase and PTE1 were detected with anti-catalase and anti-PTE1 antibodies, respectively.
(TIFF)

Figure S6 Fluorescence microscopy analysis of intracellular localization of GFP-KANL. (A) HeLa cells continuously expressing GFP-KANL were treated with control siRNA (control), VCP siRNA (nc), or PEX5 siRNA (192) for 48 hours, and then transfected with an expression vector for mCherry, VCP-mCherry, or mCherry-PEX5. Twenty-four hours later, GFP signals (green) and mCherry signals (red) were examined. (B) Quantification of fluorescence microscopy of GFP-KANL in (A).

More than 120 mCherry-positive cells were examined in each sample, and the fraction (%) of cells with diffuse GFP signals in the cytoplasm were scored. n.s., not significant.
(TIFF)

Acknowledgments

We thank Professor James A. Hejna (Kyoto University) for critical reading of the manuscript.

References

1. Vurusaner B, Poli G, Basaga H (2012) Tumor suppressor genes and ROS: complex networks of interactions. Free Radic Biol Med 52: 7–18.
2. Funato Y, Miki H (2010) Redox regulation of Wnt signalling via nucleoredoxin. Free Radic Res 44: 379–388.
3. Hu CT, Wu JR, Cheng CC, Wang S, Wang HT, et al. (2011) Reactive oxygen species-mediated PKC and integrin signaling promotes tumor progression of human hepatoma HepG2. Clin Exp Metastasis 28: 851–863.
4. Valko M, Leibfritz D, Moncol J, Cronin MT, Mazur M, et al. (2007) Free radicals and antioxidants in normal physiological functions and human disease. Int J Biochem Cell Biol 39: 44–84.
5. Legakis JE, Koepke JI, Jedeszko C, Barlaskar F, Terlecky LJ, et al. (2002) Peroxisome senescence in human fibroblasts. Mol Biol Cell 13: 4243–4255.
6. Heiland I, Erdmann R (2005) Biogenesis of peroxisomes. Topogenesis of the peroxisomal membrane and matrix proteins. FEBS J 272: 2362–2372.
7. Maynard EL, Gatto GJ Jr, Berg JM (2004) Pex5p binding affinities for canonical and noncanonical PTS1 peptides. Proteins 55: 856–861.
8. Terlecky SR, Koepke JI, Walton PA (2006) Peroxisomes and aging. Biochim Biophys Acta 1763: 1749–1754.
9. Manno A, Noguchi M, Fukushi J, Motohashi Y, Kakizuka A (2010) Enhanced ATPase activities as a primary defect of mutant valosin-containing proteins that cause inclusion body myopathy associated with Paget disease of bone and frontotemporal dementia. Genes Cells 15: 911–922.
10. Kakizuka A (2008) Roles of VCP in human neurodegenerative disorders. Biochem Soc Trans 36: 105–108.
11. Johnson JO, Mandrioli J, Benatar M, Abramzon Y, Van Deerlin VM, et al. (2010) Exome sequencing reveals VCP mutations as a cause of familial ALS. Neuron 68: 857–864.
12. Koike M, Fukushi J, Ichinohe Y, Higashimae N, Fujishiro M, et al. (2010) Valosin-containing protein (VCP) in novel feedback machinery between abnormal protein accumulation and transcriptional suppression. J Biol Chem 285: 21736–21749.
13. Mori-Konya C, Kato N, Maeda R, Yasuda K, Higashimae N, et al. (2009) p97/valosin-containing protein (VCP) is highly modulated by phosphorylation and acetylation. Genes Cells 14: 483–497.
14. Noguchi M, Takata T, Kimura Y, Manno A, Murakami K, et al. (2005) ATPase activity of p97/valosin-containing protein is regulated by oxidative modification of the evolutionally conserved cysteine 522 residue in Walker A motif. J Biol Chem 280: 41332–41341.
15. Hirabayashi M, Inoue K, Tanaka K, Nakadate K, Ohsawa Y, et al. (2001) VCP/p97 in abnormal protein aggregates, cytoplasmic vacuoles, and cell death, phenotypes relevant to neurodegeneration. Cell Death Differ 8: 977–984.
16. Kobayashi T, Tanaka K, Inoue K, Kakizuka A (2002) Functional ATPase activity of p97/valosin-containing protein (VCP) is required for the quality control of endoplasmic reticulum in neuronally differentiated mammalian PC12 cells. J Biol Chem 277: 47358–47365.
17. Chou TF, Brown SJ, Minond D, Nordin BE, Li K, et al. (2011) Reversible inhibitor of p97, DBeQ, impairs both ubiquitin-dependent and autophagic protein clearance pathways. Proc Natl Acad Sci U S A 108: 4834–4839.
18. Natsume T, Yamauchi Y, Nakayama H, Shinkawa T, Yanagida M, et al. (2002) A direct nanoflow liquid chromatography-tandem mass spectrometry system for interaction proteomics. Anal Chem 74: 4725–4733.
19. Cohen G, Rapatz W, Ruis H (1988) Sequence of the Saccharomyces cerevisiae CTA1 gene and amino acid sequence of catalase A derived from it. Eur J Biochem 176: 159–163.
20. Hartig A, Ruis H (1986) Nucleotide sequence of the Saccharomyces cerevisiae CTT1 gene and deduced amino-acid sequence of yeast catalase T. Eur J Biochem 160: 487–490.
21. Togo SH, Maebuchi M, Yokota S, Bun-Ya M, Kawahara A, et al. (2000) Immunological detection of alkaline-diaminobenzidine-negativeperoxisomes of the nematode Caenorhabditis elegans purification and unique pH optima of peroxisomal catalase. Eur J Biochem 267: 1307–1312.

Author Contributions

Conceived and designed the experiments: KM AK. Performed the experiments: KM YI MK NS S-II. Analyzed the data: KM TN AK. Contributed reagents/materials/analysis tools: NS. Wrote the paper: KM AK.

Molecular Cell
Article

The Kelch Repeat Protein KLHDC10 Regulates Oxidative Stress-Induced ASK1 Activation by Suppressing PP5

Yusuke Sekine,[1] Ryo Hatanaka,[1] Takeshi Watanabe,[1] Naoki Sono,[1] Shun-ichiro Iemura,[3,5] Tohru Natsume,[3] Erina Kuranaga,[2,4] Masayuki Miura,[2] Kohsuke Takeda,[1,6] and Hidenori Ichijo[1,*]
[1]Laboratory of Cell Signaling
[2]Department of Genetics
Graduate School of Pharmaceutical Sciences, The University of Tokyo, 7-3-1 Hongo, Bunkyo-ku, Tokyo 113-0033, Japan
[3]Biological Systems Control Team, Biomedicinal Information Research Center, National Institutes of Advanced Industrial Science and Technology, 2-42 Aomi, Koto-ku, Tokyo 135-0064, Japan
[4]Laboratory for Histogenetic Dynamics, RIKEN Center for Developmental Biology, 2-2-3 Minatojima-minamimachi, Chuo-ku, Kobe 650-0047, Japan
[5]Present address: Division of Translational Research for Drug Development, Fukushima Medical University, 1 Hikariga-oka, Fukushima-shi, Fukushima 960-1295, Japan
[6]Present address: Division of Cell Regulation, Graduate School of Biomedical Sciences, Nagasaki University, 1-14 Bunkyo-machi, Nagasaki 852-8521, Japan
*Correspondence: ichijo@mol.f.u-tokyo.ac.jp
http://dx.doi.org/10.1016/j.molcel.2012.09.018

SUMMARY

Reactive oxygen species (ROS)-induced activation of Apoptosis signal-regulating kinase 1 (ASK1) plays crucial roles in oxidative stress-mediated cell death through the activation of the JNK and p38 MAPK pathways. However, the regulatory mechanism of ASK1 in the oxidative stress response remains to be elucidated. Here, we identified the kelch repeat protein, Slim, as an activator of ASK1 through a *Drosophila* misexpression screen. We also performed a proteomics screen and revealed that Kelch domain containing 10 (KLHDC10), a mammalian ortholog of Slim, interacted with Protein phosphatase 5 (PP5), which has been shown to inactivate ASK1 in response to ROS. KLHDC10 bound to the phosphatase domain of PP5 and suppressed its phosphatase activity. Moreover, KLHDC10 was required for H_2O_2-induced sustained activation of ASK1 and cell death in Neuro2A cells. These findings suggest that Slim/KLHDC10 is an activator of ASK1, contributing to oxidative stress-induced cell death through the suppression of PP5.

INTRODUCTION

During the process of aerobic metabolism in cells, reactive oxygen species (ROS), such as superoxide anions, hydrogen peroxide (H_2O_2), and hydroxyl radicals, are produced by intracellular enzymatic systems, including the mitochondrial electron transport chain. Stressors from the exogenous environment, such as ultraviolet radiation, ionizing radiation, and anticancer drugs, also cause the formation of ROS. Excessive and/or ectopic generation of ROS results in oxidative stress, in which ROS induce nonspecific oxidation of nucleic acids, lipids, and proteins, leading to profound damage to the cells and eventually cell death. Accordingly, ROS have been considered to be the cause of various human diseases and aging. To cope with oxidative stress and maintain the intracellular homeostasis of redox status, living organisms are equipped with a wide variety of antioxidant proteins and redox-sensitive signaling systems (Finkel and Holbrook, 2000).

The mitogen-activated protein kinase (MAPK) cascades are evolutionarily conserved signaling pathways that play crucial roles in cellular responses to environmental changes (Kyriakis and Avruch, 2001; Widmann et al., 1999). Apoptosis signal-regulating kinase 1 (ASK1) is a member of the MAP kinase kinase kinases (MAP3K) that activates the c-Jun N-terminal kinase (JNK) and p38 MAPK pathways in response to a wide variety of pathophysiological stressors, including oxidative stress, endoplasmic reticulum (ER) stress, and inflammatory cytokines (Ichijo et al., 1997; Takeda et al., 2008). ASK1 has been demonstrated to be involved in ROS-induced cell death in various types of cells and has been implicated in the pathogenesis of oxidative stress-related diseases such as neurodegenerative diseases, cardiovascular diseases, and cancers (Nagai et al., 2007; Tobiume et al., 2001). The molecular mechanism of ASK1 activation by ROS has been revealed mainly through analyzing ASK1-binding proteins. Under conditions in which there is no oxidative stress, the antioxidant protein thioredoxin (Trx) forms a complex with ASK1 through the N-terminal region of ASK1, and inhibits ASK1's kinase activity (Saitoh et al., 1998). Under oxidative stress conditions, the reactive cysteine residues within Trx are oxidized and form an intramolecular disulfide bond. The oxidized form of Trx is released from ASK1, and reciprocally tumor necrosis factor (TNF) receptor-associated factor (TRAF) family proteins, such as TRAF2 and TRAF6, are recruited to ASK1 (Fujino et al., 2007; Nishitoh et al., 1998; Noguchi et al., 2005). The interaction of TRAFs with ASK1 appears to enhance

the transautophosphorylation of the threonine residue within the activation loop of the kinase domain of ASK1, which is essential for ASK1 activation (Nishitoh et al., 1998). Although Trx and TRAF family proteins are pivotal molecules in the regulation of ROS-induced activation of ASK1, we have also demonstrated that Protein phosphatase 5 (PP5) is a negative regulator of ASK1 (Morita et al., 2001). PP5 is a serine/threonine phosphatase that belongs to the Phosphoprotein phosphatase (PPP) family. It has been reported that PP5 is involved in hormone and stress responses by dephosphorylating various substrates (Golden et al., 2008; Hinds and Sánchez, 2008). PP5 interacts with the activated form of ASK1 in response to H_2O_2 and dephosphorylates the essential phosphothreonine residue, thereby inhibiting the kinase activity of ASK1 and oxidative stress- and ASK1-dependent apoptosis. Thus, PP5 is one of the key molecules that determine the cell fate in the oxidative stress response.

The kelch repeat domain consists of five to seven tandem repeats of the kelch motif and forms a β-propeller structure (Adams et al., 2000; Prag and Adams, 2003). The kelch repeat protein family members exist across species and have been reported to play roles in a wide range of cellular processes, including signal transduction, transcription, DNA repair, and protein degradation. Because the kelch repeat domain is important for protein-protein interactions, the kelch repeat proteins function mainly through interaction with their binding partners. Recently, several lines of evidence have demonstrated that the kelch repeat proteins interact with the complex-type ubiquitin E3 ligases called the Cullin-RING ligases (CRLs) and serve as the substrate recognition subunits of the CRL complex, which determine the substrate specificity of this complex (Bennett et al., 2010). However, the molecular functions and physiological roles of most kelch repeat proteins remain unknown.

Here, we identified the kelch repeat protein Slim and its mammalian ortholog KLHDC10 as an activator of ASK1 by taking advantage of *Drosophila* genetics. Slim/KLHDC10 was found to activate ASK1 through the suppression of PP5 and thereby to contribute to oxidative stress-induced cell death.

RESULTS

A Misexpression Screen for Activators of ASK1 using *Drosophila*

To identify genes that regulate activation of the ASK1-MAPK cascades, we took advantage of a *Drosophila* misexpression screen, using the GAL4/UAS system that has been extensively used to induce ectopic gene expression in flies (Brand and Perrimon, 1993). We have recently reported that an N terminus-lacking mutant of *Drosophila* ASK1 (DASK1 ΔN) activated the *Drosophila* p38 (Dp38) pathway more strongly than did DASK1 wild-type (WT) (Sekine et al., 2011). Ectopic expression of DASK1 ΔN, but not DASK1 WT, under the control of *pannier* (*pnr*)-*GAL4*, which is expressed along the dorsal midline of adult flies, resulted in a Dp38-dependent increase in melanization (increase in black and brown pigments) in the thorax cuticle of flies (Figures 1A and 1B) (Sekine et al., 2011). To establish a misexpression screening system for activators of ASK1, we used this melanization as a visible marker for activation of the ASK1-p38 pathway in flies and sought to screen for genes that could induce melanization in the thorax in a *pnr-GAL4*-dependent manner. The Gene Search (GS) lines have a GS vector that contains UAS, which is randomly inserted in the fly genome of each GS line, thereby allowing ectopic expression of endogenous genes after crossing with the GAL4 driver strains (Toba et al., 1999). We generated *pnr > DASK1WT* flies and crossed them with approximately 4,500 GS lines. The melanization of thoraxes of the F1 progeny was examined, and nine lines were found to exhibit enhanced melanization in a *pnr-GAL4*-dependent manner. We designated those lines as *kuma* (*key upswing in melanin accumulation*) lines.

Slim Expression in *pnr > kuma1* Flies Induces Melanization

Of the nine *kuma* lines, we focused on the *kuma1* (GS10238) line. All of the *pnr > kuma1* flies exhibited strong melanization, similar to *pnr > DASK1ΔN*, even without coexpression of DASK1 WT (Figure 1C). These results suggest that *kuma1*-dependent activation of endogenous DASK1-Dp38 may be sufficient to melanize the thorax in these conditions. When we crossed the flies at 18°C (a temperature that weakly induced the gene misexpression in *kuma1*), about half of the *pnr > kuma1* flies showed a weak phenotype that resulted in the loss of the upper half of melanization in the thoracic *pnr-GAL4* expression region (indicated by the white arrowhead in Figure 1D). Under these conditions, coexpression of DASK1 WT restored the melanization in *pnr > kuma1* flies, suggesting that exogenous DASK1 enhanced the melanization in *pnr > kuma1* flies (Figure 1D). The GS vector in the *kuma1* line was inserted 508 bases upstream of a gene, *scruin like at the midline* (*slim*) (Figure 1E), and we examined the expression levels of *slim* in *kuma1* lines under the control of heat shock (hs)-inducible GAL4. The expression of *slim* mRNA in *hs > kuma1* flies was elevated compared to that in *hs > GFP* flies, whereas the expression levels of *DASK1* or *CG5189*, which is located directly 3′ to *slim*, were not affected (Figure 1F). Slim protein levels were also increased in *hs > kuma1* flies (Figure 1G). Furthermore, coexpression of inverted repeat (IR) RNA targeting *slim* (*slim-IR*) strongly reduced the melanization in *pnr > kuma1* flies (Figures 2A and 2B). Based on these results, we concluded that *slim* is the gene responsible for melanization in the thorax of *pnr > kuma1*.

The DASK1-Dp38 Pathway Mediates Slim-Induced Melanization

Because DASK1 ΔN-induced melanization is dependent on the Dp38 pathway (Sekine et al., 2011), we examined the requirement of the DASK1-Dp38 pathway for Slim-induced melanization. IR RNA-mediated knockdown of *DASK1* or *licorne (lic)*, a *Drosophila* MAP2K gene in the Dp38 pathway, in *pnr > kuma1* flies partially inhibited melanization (Figures 2C and 2D). In addition, the expression of a dominant-negative mutant of Dp38a (Dp38a DN) also reduced melanization in *pnr > kuma1* flies (Figure 2E). By contrast, knockdown of *slim* did not affect DASK1 ΔN-induced melanization (Figures 2F and 2G), indicating that *slim* is genetically located upstream of *DASK1* and that Slim-induced melanization was mediated through the DASK1-Dp38 pathway.